Ocean Modelling 38 (2011) 96–113

Contents lists available at ScienceDirect

Ocean Modelling

journal homepage: www.elsevier.com/locate/ocemod

Nested and multi-physics modeling of tsunami evolution from generation to inundation

Sangyoung Son [a], Patrick J. Lynett [a,*], Dae-Hong Kim [b]

[a] Zachry Department of Civil Engineering, Texas A&M University, College Station, TX 77843-3136, United States
[b] Department of Civil Engineering, University of Seoul, 130-743, Republic of Korea

ARTICLE INFO

Article history:
Received 30 September 2010
Received in revised form 8 February 2011
Accepted 17 February 2011
Available online 24 February 2011

Keywords:
Shallow water equations
Boussinesq equations
Coupling
Coherent structures
Turbulence
Tsunami

ABSTRACT

This paper aims to introduce non-dispersive shallow water and dispersive, Boussinesq-type numerical models used in tsunami modeling, as well as an approach to two-way couple these models together. The fundamental purpose of the coupling effort is to develop the capability to seamlessly model tsunami evolution from generation to inundation with fine scale resolution, without the loss of locally important physics. The two model components are briefly introduced, and the physical mismatch between the two models is examined analytically. As coupling of numerically and physically heterogeneous models may result in undesirable errors, a general benchmark test has been undertaken to provide a parameter range for expected accuracy and stability. Long wave propagation onto a shallow shelf is simulated to validate the coupled model, examining the importance of dispersive and nonlinear effects in the nearshore area, as well as the utility of the coupled modeling system. Finally, the model is applied to the 2004 Indian Ocean tsunami. In this test, the local dynamics experienced in the Port of Salalah in Oman, as documented by Okal et al. (2006), are recreated.

1. Introduction

As a long gravity wave propagates over a non-uniform ocean bottom, shoaling and refraction can have a transforming effect. The response of waves to bathymetric changes results in deformation of the amplitude and wavelength, permitting waves to conserve mass and momentum. Many efforts have been made to construct a relationship between wave height and water depth, and using various levels of approximation (e.g., linear waves) it is possible. For the approximation of long and intermediate length (or shallow and intermediate depth) waves, two physical characteristics of waves, nonlinearity and frequency dispersion, are generally employed.

Under a "true" long wave, frequency dispersion is negligible. This assumption yields a hydrostatic pressure field and a horizontal velocity that is uniform over depth. A tsunami is often considered a long wave. Frequency dispersion in a tsunami can be ignored when the tsunami wavelength, typically on the order of 100 km in the deep ocean, is considerably larger than water depth. Therefore, the usual approach to describe tsunami evolution is to take either the linear or nonlinear shallow-water models as the governing equations. A number of computational models based on this approximation exist, and some are introduced here. Method of splitting tsunami (MOST) developed by Titov and Synolakis (1998) is capable of predicting wave height or inundation using a technique where two-dimensional equations are split into a pair of one-dimensional equations. Liu et al. (1998), on the other hand, presented Cornell multi-grid coupled tsunami model (COMCOT) adopting the staggered leap-frog integration with an upwind scheme for the nonlinear convective terms. COMCOT can also model tsunami propagation and some nearshore-dynamics such as run-up. Global tsunami model (GTM) was designated for assessment of tsunami hazard, inundation, mapping and prediction of the tsunami arrival time by Kowalik et al. (2005). More recently, aided by adaptive finite volume methods for wave propagation, TsunamiClaw (Conservation Laws) has been created as a work of George and LeVeque (2006). Lastly, TsunAWI uses the finite element method with the advantage of flexibility in grid generation, and was found to be comparable to the multi-grid, nested modeling approach (Harig et al., 2008).

Even though all of these models employ different numerical techniques, all solve the linear and/or nonlinear shallow water equations. Depending on the wavelength of the tsunami, however, frequency dispersion effects can be significant. Specifically, neither hydro-static pressure nor depth-constant horizontal velocity can be presumed. For transoceanic propagation of a tsunami as well as landslide-generated tsunami, the dispersive effects, estimated through the ratio of water depth to wavelength, should be included to yield more accurate results (e.g., Yoon, 2002; Lynett et al., 2003; Grilli et al., 2007). For this reason, some efforts to add the frequency dispersion effect into non-dispersive models through numerical truncation error have been made (e.g., Yoon, 2002;

* Corresponding author. Tel.: +1 979 862 3627.
E-mail address: plynett@tamu.edu (P.J. Lynett).

1463-5003/$ - see front matter © 2011 Elsevier Ltd. All rights reserved.
doi:10.1016/j.ocemod.2011.02.007

Burwell et al., 2007). Despite such attempts to mimic physical dispersion, it is still an attractive challenge to model tsunami with the Boussinesq or Navier–Stokes equations with the aim to, hopefully, obtain more realistic wave predictions. Corresponding examples include Cornell University long and intermediate wave modeling package (COULWAVE) by Lynett et al. (2003), GEOWAVE, which is equipped with the fully nonlinear wave model (FUNWAVE) engine, by Grilli et al. (2007), and recent work by Saito and Furumura (2009).

The above mentioned computational models aim, of course, for accurate prediction of nearshore physics such as wave shoaling, wave-diffraction and refraction, run-up and nonlinear interactions of waves, each with their specialized advantages, e.g., small computational time of COMCOT or rigorous representation of physics in the Boussinesq model. In coastal regions, where the water depth is very shallow and amplitude and wavelength can become high and short, nonlinear and bathymetric interactions across a wide range of frequencies occur. These interactions can locally generate various shorter-crested, or dispersive waves components. A well known example is the transformation of a tsunami front into an undular bore. Thus, the nearshore is expected to be nonlinear and (possibly) dispersive, and Boussinesq model is appropriate, as addressed in some literature (e.g., Lynett, 2006). In related efforts, Kim et al. (2009) have presented a depth-integrated model for weakly dispersive, turbulent and rotational fluid flows. This approach permits the explicit inclusion of viscous effects in shallow water, coupled with the nonlinear and weakly-dispersive physics of the Boussinesq model. With accuracy, this model can simulate nonlinear and weakly dispersive nearshore dynamics, as well as large eddies generated by long waves and currents.

Here it is postulated that a more physically complete attempt at tsunami modeling can be achieved through the integration of a shallow water equation model with a Boussinesq model. COMCOT is computationally "in charge" of generation and propagation of tsunamis in the deep, open ocean, which in general will be the huge majority of a simulation domain. On the other hand, the Boussinesq effort can be concentrated on a specific area of interest, typically nearshore where waves are prone to high nonlinearity, turbulence, and local frequency dispersion.

This paper aims to introduce a set of numerical models used in tsunami modeling, as well as a method to couple them together. The fundamental purpose of the coupling effort is to develop the capability to seamlessly model tsunami evolution from generation to inundation with fine scale resolution, without the loss of locally relevant physics. In addition to this, local turbulent structures, such as eddies and gyres, generated by tsunamis in the nearshore area or around coastal structures can be studied with the coupled model.

The outline of this paper is as follows. In the first two sections, the model components, the shallow water wave equation model (COMCOT) and the Boussinesq-type model, will be briefly introduced with their numerical scheme. Physical and numerical "mismatches" between the two models will be discussed analytically, which is followed by the coupling method given in detail. The next section is devoted to the validation of the coupled model through a benchmark test with wide-varying conditions and resulting guidance for general use. A typical problem of long wave propagation into the coast is given in following section. Finally, the presented model is applied to the 2004 Sumatra tsunami to investigate nearshore dynamics, with a particular focus on the eddies generated inside a harbor basin.

2. Shallow water equation model

As introduced above, Liu et al. (1998) presented a nested multigrid model which has the option of using either the linear or the nonlinear shallow water equations (NLSW) with two different types of coordinate systems, namely Cartesian or spherical. This general framework includes the effects of bottom friction as well as a special treatment for the moving shoreline. The model named COMCOT v.1.6 has been adapted here to simulate tsunami propagation across oceanic basins.

2.1. Governing physics

The nonlinear shallow equations including bottom frictional effects in conservative form are:

$$\frac{\partial \zeta}{\partial t}+\frac{\partial M}{\partial x}+\frac{\partial N}{\partial y}=0, \tag{1}$$

$$\frac{\partial M}{\partial t}+\frac{\partial}{\partial x}\left(\frac{M^2}{H}\right)+\frac{\partial}{\partial y}\left(\frac{MN}{H}\right)+gH\frac{\partial \zeta}{\partial x}+\tau_x=0, \tag{2}$$

$$\frac{\partial N}{\partial t}+\frac{\partial}{\partial x}\left(\frac{MN}{H}\right)+\frac{\partial}{\partial y}\left(\frac{N^2}{H}\right)+gH\frac{\partial \zeta}{\partial y}+\tau_y=0, \tag{3}$$

in which ζ is the surface elevation, h is the still water depth, $H = h + \zeta$ is the total water depth, and M, N are the volume fluxes in the x and y directions, defined respectively as Hu and Hv. The bottom friction terms τ_x, τ_y in the momentum equations are approximated in COMCOT via Manning's formulation:

$$\tau_x=\frac{gm^2}{H^{7/3}}M(M^2+N^2)^{1/2}, \tag{4}$$

$$\tau_y=\frac{gm^2}{H^{7/3}}N(M^2+N^2)^{1/2}, \tag{5}$$

where m is the Manning's relative roughness coefficient. Note that the above equation set is the nonlinear solver in COMCOT; the linear solver of course neglects the convection terms in the momentum equations, and does include the Coriolis force when solving in spherical coordinates.

2.2. Numerical scheme

The numerical scheme employed by COMCOT is the explicit leap-frog difference method. Nonlinear terms in the model are approximated with upwind finite differences and linear terms by two-point centered finite differences. This numerical scheme is stable and robust but is a low-order accurate method, meaning that it is susceptible to numerical dispersion and dissipation errors. The finite difference forms for the continuity and momentum equations are described in Appendix A. The finite difference stencil of this scheme is depicted in Fig. 1, suggesting two neighboring points on each side of a calculation point are necessary for each location calculation of derivatives.

For the present study, COMCOT has been parallelized for use on shared-memory computers, such as multi-processors and/or multi-core computers. OpenMP was used for the parallelization, which is the standard method for shared-memory parallelization. The parallel model has been tested up to 8 processors, and shows a near linear speed-up (using 8 processors reduces CPU time by a factor of 1/8).

To generate the tsunami from an undersea earthquake, COMCOT uses the fault model of Okada (1985). The main assumptions of this model are a rectangular fault plane within an elastic deformation. The fault model predicts the deformation of the seafloor, which corresponds directly to the initial deformation of the ocean water free surface. Once the earthquake has been described with the above parameter set, COMCOT is able to propagate the initial disturbance across oceans. For propagation across deep ocean waters, COMCOT gives the option of using the linear version of the shallow water equations. This version is solved considerably

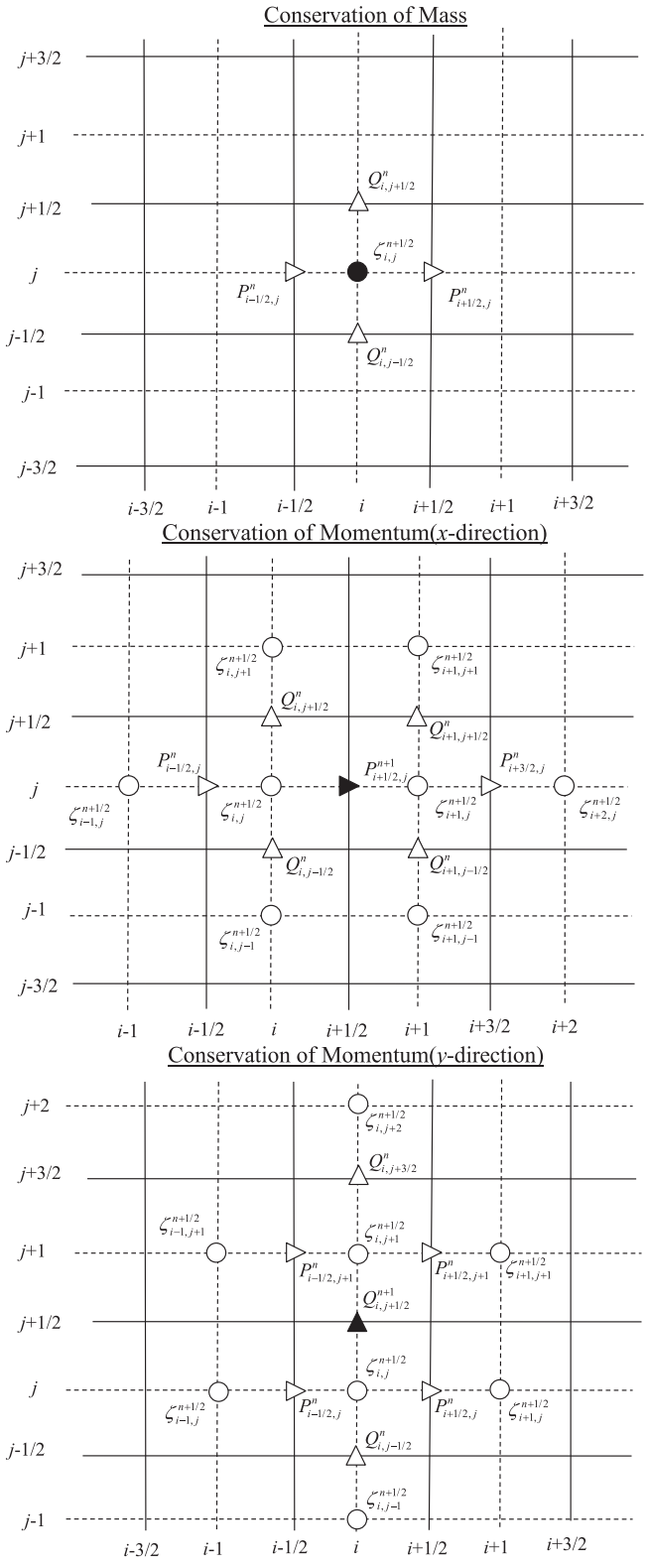

Fig. 1. Finite difference stencils for COMCOT.

faster, in the computational sense, than the nonlinear version, and can be used with confidence as long as the tsunami wave height is a very small fraction of the depth, practically less than 1/25–1/50 of the local depth. When this threshold is exceeded, the nonlinear version of COMCOT is required for accurate results. Generally, if runup or nearshore wave heights are needed, the nonlinear version of the model should be used.

For runup calculations, COMCOT utilizes a simple but accurate moving shoreline algorithm. The continuously sloping beach profile is approximated as a stair-stepped profile. When the water level exceeds the elevation of the "stair" above, the water floods that "step" and the shoreline moves landward (inundation). This approach has shown to re-produce analytical solutions reasonably and field data as well as any other published, shallow-water equation model.

3. Boussinesq equation model

Recently, Kim et al. (2009) have presented a depth-integrated model for weakly dispersive, turbulent and rotational fluid flows. It is derived from the spatially-filtered Navier–Stokes equations in order to consider viscous effects of a turbulent fluid. Accordingly, this model includes approximated bottom-induced turbulence and thereby the associated vertical and horizontal rotational effects can be captured. In the present study, we have adopted the Boussinesq model of Kim et al. (2009) to simulate the nearshore hydrodynamics and turbulence effects such as large eddies and wakes generated in the nearshore.

3.1. Governing physics

The Boussinesq-type equations including turbulent viscosity and the associated horizontal and vertical vorticity terms are given in conservative form below:

$$\frac{\partial H}{\partial t}+\frac{\partial HU_\alpha}{\partial x}+\frac{\partial HV_\alpha}{\partial y}+D_c=0, \tag{6}$$

$$\frac{\partial HU_\alpha}{\partial t}+\frac{\partial HU_\alpha^2}{\partial x}+\frac{\partial HU_\alpha V_\alpha}{\partial y}+gH\frac{\partial \zeta}{\partial x}+HD_m^x+U_\alpha D_c=0, \tag{7}$$

$$\frac{\partial HV_\alpha}{\partial t}+\frac{\partial HU_\alpha V_\alpha}{\partial x}+\frac{\partial HV_\alpha^2}{\partial y}+gH\frac{\partial \zeta}{\partial y}+HD_m^y+V_\alpha D_c=0, \tag{8}$$

where U_α and V_α are the x and y component velocities at $z_\alpha = -0.531$ h and D_m^x, D_m^y are 2nd order correction terms of the depth-integrated momentum equations as defined in Kim et al. (2009). Likewise D_c includes 2nd order correction terms in the continuity equation. It is noted that the dispersive, viscous, and vorticity corrections are included as these 2nd order terms. All 2nd order terms can be found in Appendix B.

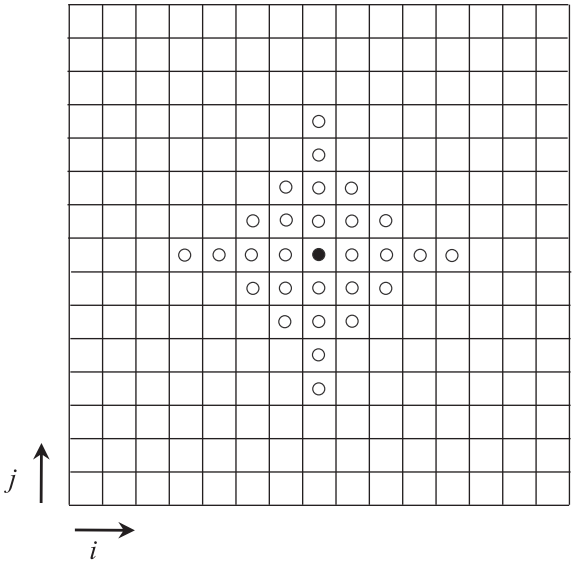

Fig. 2. Finite volume stencil for Boussinesq model.

3.2. Numerical scheme

To numerically solve the governing equations in conservative form, a highly accurate and stable model is developed. The numerical method uses a fourth-order monotone upstream-centered schemes for conservation laws–total variation diminishing (MUSCL-TVD) to solve the leading order (shallow water) terms, while for the dispersive terms, a cell averaged finite volume method is implemented. For the time integration, a third order Adams–Bashforth predictor and the fourth-order Adams–Moulton corrector scheme has been used to keep numerical truncation errors small. It is noted that Boussinesq-type models such as the one

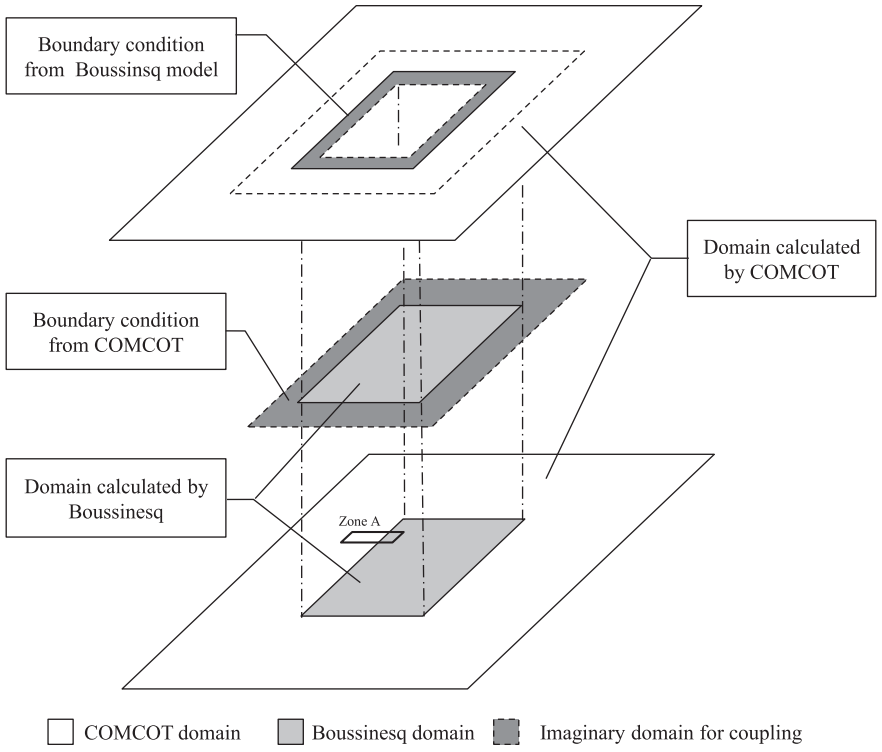

Fig. 3. Schematic drawing of coupled grid system ("Zone A" is specified for Fig. 4).

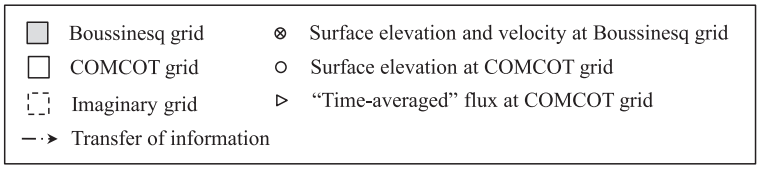

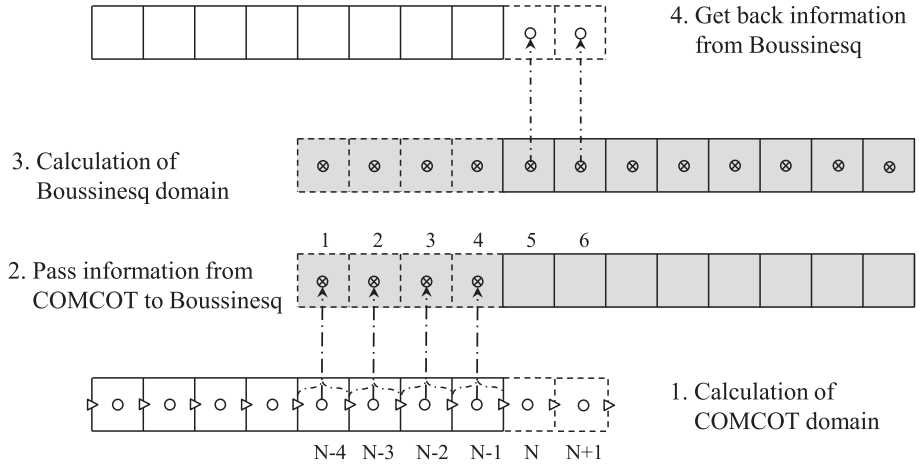

Fig. 4. Data exchange schematic between COMCOT and Boussinesq grids (detailed view of "Zone A" in Fig. 3).

solved here, which include up to third-order spatial derivatives, require a high-order solution scheme to keep the derivatives associated with the numerical truncation error at least an order below those contained in the model equations.

The explicit predictor step is

$$\zeta^{n+1} = \zeta^n + \frac{\Delta t}{12}\left(23E^n - 16E^{n-1} + 5E^{n-2}\right), \tag{9}$$

$$P^{n+1} = P^n + \frac{\Delta t}{12}\left(23F^n - 16F^{n-1} + 5F^{n-2}\right) + 2F_1^n - 3F_1^{n-1} + F_1^{n-2} + F_v^p, \tag{10}$$

$$Q^{n+1} = Q^n + \frac{\Delta t}{12}\left(23G^n - 16G^{n-1} + 5G^{n-2}\right) + 2G_1^n - 3G_1^{n-1} + G_1^{n-2} + G_v^p. \tag{11}$$

The implicit corrector step is

$$\zeta^{n+1} = \zeta^n + \frac{\Delta t}{24}\left(9E^{n+1} + 19E^n - 5E^{n-1} + E^{n-2}\right), \tag{12}$$

$$P^{n+1} = P^n + \frac{\Delta t}{24}\left(9F^{n+1} + 19F^n - 5F^{n-1} + F^{n-2}\right) + F_1^{n+1} - F_1^n + F_v^c, \tag{13}$$

$$Q^{n+1} = Q^n + \frac{\Delta t}{24}\left(9G^{n+1} + 19G^n - 5G^{n-1} + G^{n-2}\right) + G_1^{n+1} - G_1^n + G_v^c, \tag{14}$$

where P, Q are defined as:

$$P = HU_\alpha + \frac{H}{2}(z_\alpha^2 - \zeta^2)U_{\alpha xx} + H(z_\alpha - \zeta)(hU_\alpha)_{xx} - H\zeta_x\{\zeta U_{\alpha x} + (hU_\alpha)_x\}, \tag{15}$$

$$Q = HV_\alpha + \frac{H}{2}(z_\alpha^2 - \zeta^2)V_{\alpha yy} + H(z_\alpha - \zeta)(hV_\alpha)_{yy} - H\zeta_y\left\{\zeta V_{\alpha y} + (hV_\alpha)_y\right\}, \tag{16}$$

where the superscript n denotes time level and the subscripts x and y imply derivatives in the x and y direction, respectively. E, F, G, F_1, G_1, $F_v^p, G_v^p, F_v^c, G_v^c$ in the above equations include a number of spatially discretized terms; all can be found in Appendix B. The finite volume stencil for this scheme is displayed in Fig. 2, which shows that 4 neighboring points are required for each local calculation.

4. Preliminary discussion for mismatches between models

It is necessary to compare models in terms of both physical limitations and numerical properties, as this will provide the basic

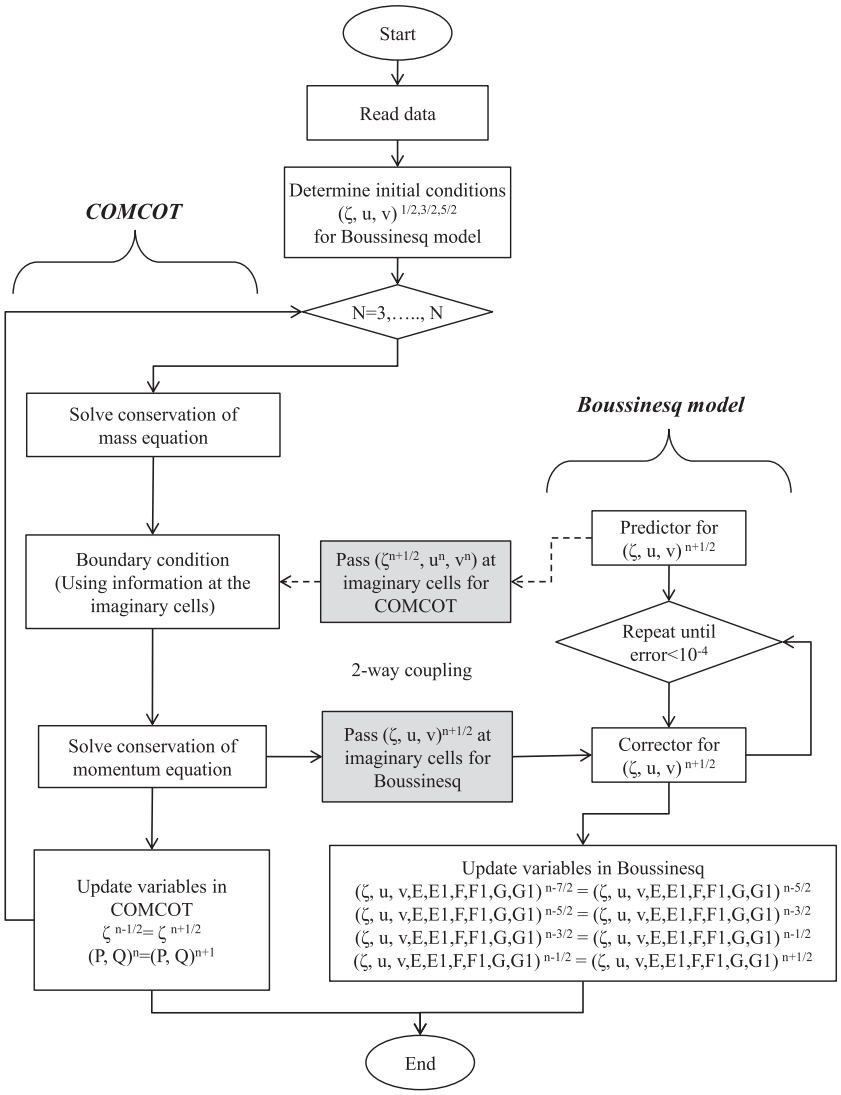

Fig. 5. Flowchart of coupled COMCOT–Boussinesq model calculations.

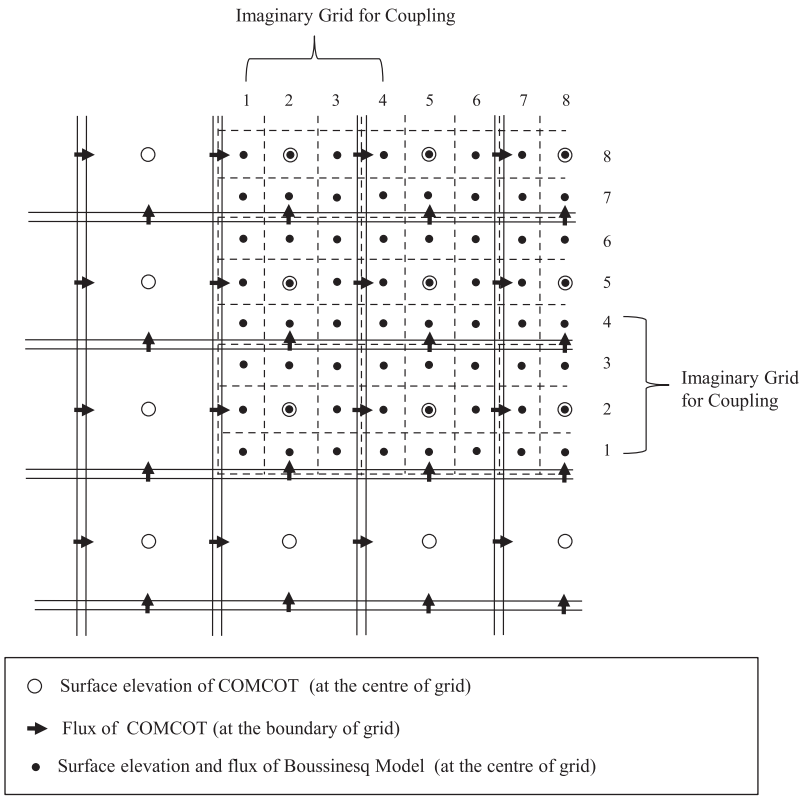

Fig. 6. Grid system for different grid sizes between COMCOT and Boussinesq model (lower-left corner section only).

guidance for coupling. There exist two major groups of errors, one from approximated equations and the other from the numerical scheme, the so-called truncation error. Prior to our coupling work, we shall thus consider the physical and numerical differences between COMCOT and the Boussinesq model, since the models, of course, have different governing equations as well as very different numerical solution schemes, which will cause a physical and numerical accuracy mismatch along the coupling interface.

4.1. Mismatch in physics

COMCOT, based on the shallow water equations, approximates the horizontal velocities and pressure gradient to be constant with depth, so one can ignore vertical variation of physics. On the other hand, Boussinesq-type equations allow (weak) vertical change of horizontal velocity, expressed as quadratic function of z. This allowance of vertical variation in the flow permits the model to include the effects of frequency dispersion. In addition to this, Kim et al. (2009) included viscous and rotational effects, which originate from bottom-induced stress. Both frequency dispersion and viscous effects exist as corrections to the leading order terms-the inviscid nonlinear shallow water equations. This can be seen straightforwardly by eliminating 2nd order terms in Eqs. (6)–(8) and then comparing with Eqs. (1)–(3). Also note that the bottom friction terms in both models are included, but in a different manner; COMCOT has ad hoc added friction terms in the momentum equations, while the Boussinesq model has both the bottom stress and a number of additional terms resulting from an explicit inclusion of bottom stress in the derivation. Consequently, in order to avoid errors from these physical differences, dispersive and viscous effects should be sufficiently small in order for governing physics to be continuous across the model interface. In other words, physics-driven model errors can be mitigated when the local relative depth (h/L) and bottom friction along interface are small. Of course

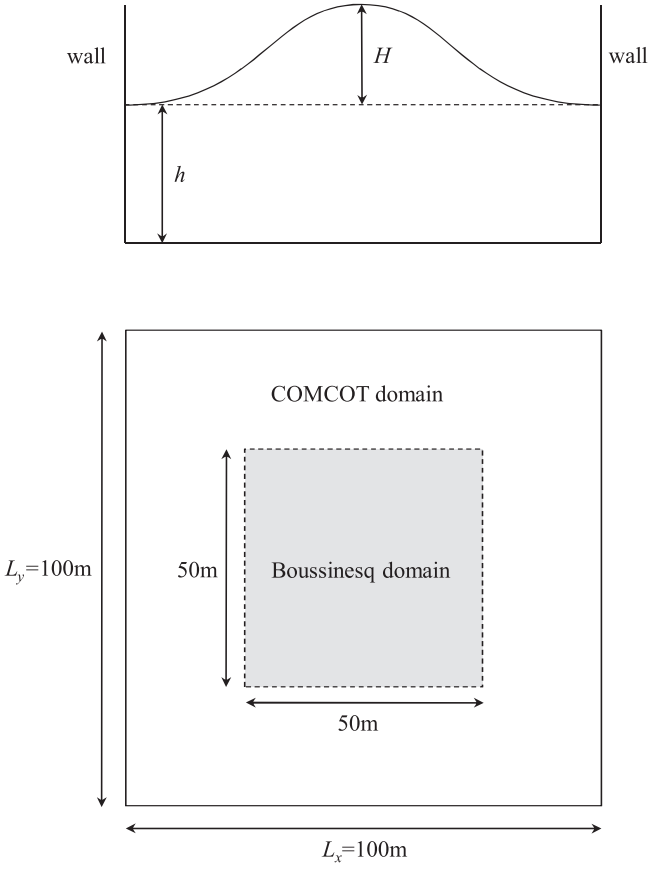

Fig. 7. Physical concept of Gaussian hump simulations; top: front view, bottom: plan view.

in a general, nonlinear simulation, one can not for example guarantee the minimum simulated value of L a priori, but such relations can be used as guidance for constructing a simulation.

4.2. Mismatch in numerics

Different numerical solution schemes will produce different output even if solving the same algebraic equations. Discretizing equations using any sort of numerical method includes an error from truncation, and such errors of course depend on the numerical scheme itself. As explained in the previous section, COMCOT and the Boussinesq model employ different types of schemes; while both are fixed grid solvers, the spatial stencils of the two schemes are very different, as are the time integration methods.

Again, the Boussinesq solver is a fourth-order accurate scheme and COMCOT a second-order scheme. Since all numerical truncation errors from the Boussinesq solver are at least two orders of differentiation higher than those from the COMCOT solver, the primary numerical error will originate from the nonlinear COMCOT model. Specifically, the leading order truncation error arising from the upwind differencing can be given as:

$$Er = 0.5(1 - Cr)u\Delta x\frac{\partial^2 u}{\partial x^2}, \tag{17}$$

where Er is the numerical truncation error of the upwind difference and Cr is the local courant number, given as $(\Delta t\sqrt{gh})/\Delta x$. In general, it is not possible to ensure $Cr \approx 1$ in COMCOT for an arbitrary grid with variable bathymetry, and furthermore the maximum allowable Cr in the COMCOT scheme according to stability analysis is 0.7 (in the Boussinesq it is 0.5 according to Kim et al. (2009)). It is reasonable to assume that $Er \approx O\left(u\Delta x\frac{\partial^2 u}{\partial x^2}\right)$ for a generic geophysical simulation. Thus, the only solution to ensure a precise numerical match across the coupling interface is to have a true long wave, with negligible depth-averaged velocity curvature in the horizontal plane, at the interface location. This conclusion is not surprising, as the shallow water based COMCOT model has this as a general requirement for accuracy in any and all applications. By requiring that, at the interface, the physics represented by COMCOT are valid for that location, the mismatch in numerics essentially vanishes. If one was able to isolate the dispersive and viscous effects in the Boussinesq domain, and such effects were small at the coupling interface, the model matching would be best.

From the above discussion, it can be reasonably expected that the primary errors expected at the coupling interface are driven by physical differences in the model equations, and specifically use of the COMCOT model for a hydrodynamic situation where it is, strictly speaking, beyond its physical validity limits. Note that possibly large numerical differences might also exist; however as discussed above these arise when the wave is not practically long, and the velocity curvature is not negligible. This expectation implies that some sort of special treatment to deal with the physics mismatch will be required at the interface. This will be described in more detail in the next session. The general approach will be to turn "off" of the high order terms in the Boussinesq model at the interface and slowly turn them back "on" as one moves inside the Boussinesq domain. The remaining model mismatch errors, controlled by slightly different viscous closures and very different numerical schemes, will be mitigated by spatial filtering. Stability and accuracy of this special treatment will be discussed as well.

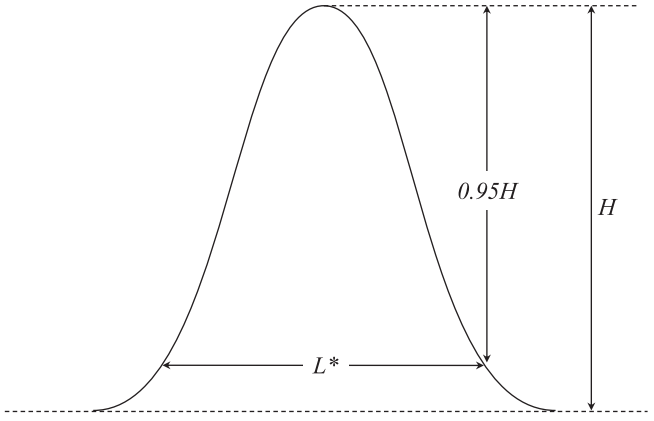

Fig. 8. Definition sketch for L^*.

5. Coupling approach

The coupling method in which the shallow water model and Boussinesq model are integrated is presented here. The constituents are two-way coupled. Boundary conditions on the interfacing side of each model are provided by its counterpart model through data exchange and overlapping grid points.

5.1. Coupling method

To accommodate data exchange between the two models, the computational grids of both models should be overlapping, as shown in Fig. 3. Since each model has derivatives of different order in the corresponding governing equations, they each need a different number of overlapping points. These overlapping points act as exterior boundary conditions on the spatial edges of the computational domain; they are effectively imaginary grid points with data values taken from the neighboring model. As seen in Fig. 4, COMCOT needs two points as a boundary condition whereas the Boussinesq model requires four neighboring points due to the 4th order MUSCL-TVD scheme and 3rd order spatial derivatives. Also, special attention must be paid to the calculation of velocity as each model defines velocity (or flux) at a different location relative to a cell (grid points are defined at the center of a cell). In the Boussinesq model, surface elevation as well as velocity components are defined at the center of the cell. On the other hand, flux has been placed at the interface of each cell in COMCOT model due to the staggered grid.

With this concept of the interface treatment, we propose the calculation algorithm as shown in Fig. 5. The algorithm consists of two main parts. The first part is the COMCOT model calculation on the left side of Fig. 5 and the other is the Boussinesq model calculation on the right side. They exchange data every time step through two-way coupling, as indicated by the boxes in the middle of Fig. 5.

The coupling algorithm can be explained in more detail by proceeding step by step. Let it be assumed that information up to time level $t = t_n$ is known. Note that the numerical scheme of COMCOT is staggered not only in space but also in time. Therefore in COMCOT, flux is known at time level $t = t_n$ and the surface elevation at time level $t = t_{n-1/2}$. For the Boussinesq model, the surface elevation and velocities at time level $t = t_{n-1/2}$ are known. All dependent variables in the Boussinesq model are calculated at the same time level,

Table 1
Simulation setup.

r	ϵ	Cr	e
1	0.001	0.01	1
2	0.01	0.05	2
4	0.1	0.1	5
6	1	0.5	10
10	–	–	–

$t = t_{n+1/2}$, whereas COMCOT simulates the surface elevation and flux terms at the time level $t = t_{n+1/2}$ and $t = t_{n+1}$, respectively, following the leap frog scheme. The coupled solution scheme is outlined below.

1. Calculate COMCOT free surface at time level $t = t_{n+1/2}$ by solving the NLSW continuity equation with flux information at time level $t = t_n$ and surface elevation at time level $t = t_{n-1/2}$.
2. Calculate all predictor step values in the Boussinesq model, yielding initial predictions at time level $t = t_{n+1/2}$ for surface elevation as well as velocity.
3. Transfer predictor Boussinesq surface elevation values and fluxes along the interface at time level $t = t_{n+1/2}$ and $t = t_n$, respectively, into COMCOT as boundary conditions. Note that Boussinesq flux term should be interpolated not only spatially but also in time. Linear one-dimensional interpolation is used, numerically consistent with the upwind differencing in COMCOT. If the grid size in each model is not constant, utilize a two-dimensional (bi-linear) interpolation technique to give appropriate boundary condition at the interface.
4. Calculate the COMCOT flux at time level $t = t_{n+1}$ by solving the shallow water momentum equation with surface elevation information at time level $t = t_{n+1/2}$ along with flux at time level $t = t_n$. In this step, the information transferred from Boussinesq model has been used.
5. Extract the boundary condition at time level $t = t_{n+1/2}$ to be transferred from COMCOT into the Boussinesq model. Again, note that the Boussinesq model does not employ a staggered-grid in time. Having already calculated the COMCOT surface elevation at time level $t = t_{n+1/2}$, our interest will focus on getting the COMCOT flux at time level $t = t_{n+1/2}$. This can be done simply by taking average two values both at time level $t = t_n$ and $t = t_{n+1}$.
6. Transfer the COMCOT surface elevation and flux along the interface at time level $t = t_{n+1/2}$ into the Boussinesq as boundary conditions required for the implicit corrector step.
7. Calculate the surface elevation and velocities at $t = t_{n+1/2}$ from the Boussinesq corrector using COMCOT boundary conditions at time level $t = t_{n+1/2}$.
8. Optionally, a filtering technique can be applied in order to remove spurious two-grid wave components with high frequency. See Section 5.3 below for details.
9. Return to step 1 for the next time step.

5.2. Coupling with different grid size

Coupling with different grid sizes can also be accommodated. For the estimation of information at an interface, an interpolation technique has been used. If the relative position of a desired point in a grid is known, f_a at the desired point (x_a, y_a) is calculated by using bilinear interpolation as follows:

$$f_a = (1-t)(1-u)f_{BL} + t(1-u)f_{BR} + tuf_{TR} + (1-t)uf_{TL}, \tag{18}$$

in which:

$$t \equiv \frac{x_a - x_L}{x_R - x_L}, \quad u \equiv \frac{y_a - y_B}{y_T - y_B}, \tag{19}$$

where the subscript L, R, B and T in the above definition respectively means left, right, bottom and top. Fig. 6 shows the grid system for coupling with different grid sizes.

5.3. Special numerical interface treatment

Each of the two numerical models coupled here has its own governing equations (approximated physics) and numerical scheme, and this can result in both a physical and numerical mismatch along the interface, as discussed above. From a qualitative analysis of the equations and numerical differences, it is extrapolated that large numerical differences arise only when significant equation (physics) differences exist. This expectation was observed during early testing of the interface. To reduce this primary error dependency on the mismatch of model physics, the high-order dispersive terms in the Boussinesq model are neglected at the interface. These terms are linearly ramped back into the equations over a length of 20 grid points moving away from the COMCOT interface.

While forcing the two numerical schemes to solve similar governing equations at the interface eliminates a large fraction of the interface error, the different viscous treatments and numerical solvers will still incur some error in the simulation. This error commonly takes the form of spurious high-frequency, two-grid wave components; in essence numerical noise reflected off "improper" boundary conditions. To remove this spurious two-grid wave component, the nine-point spatial filter is employed as suggested in Shapiro (1970).

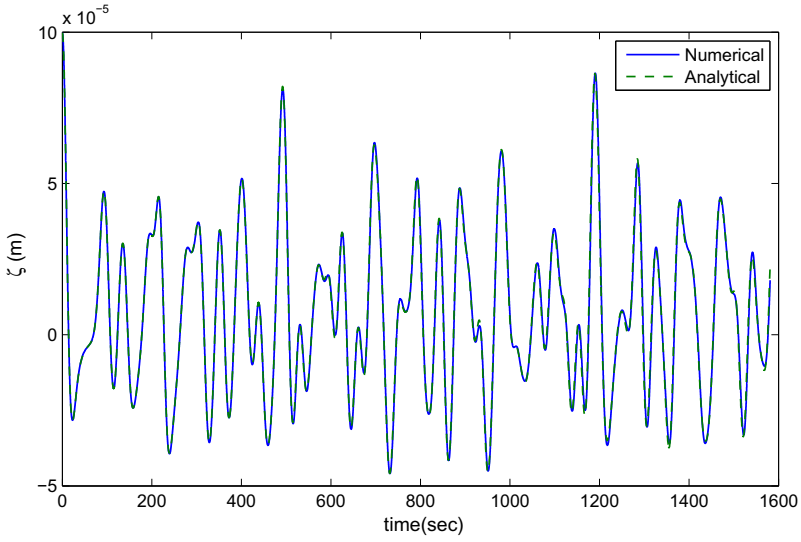

Fig. 9. Temporal variation of free surface elevation at the center of the wave basin ($r = 1, \epsilon = 0.001, Cr = 0.01$ and $e = 10$).

$$\zeta_i = \frac{1}{256}\{186\zeta_i + 56(\zeta_{i-1} + \zeta_{i+1}) - 28(\zeta_{i-2} + \zeta_{i+2}) + 8(\zeta_{i-3} + \zeta_{i+3}) - (\zeta_{i-4} + \zeta_{i+4})\}. \quad (20)$$

Note that application of this filter is common in high-order Boussinesq applications, which tend to be prone to high frequency instability (e.g., Gobbi and Kirby, 1999), and is not used in the COMCOT domain. The filter is typically applied throughout the entire Boussinesq domain once every 100 time steps.

6. Validation

As discussed above, coupling of two heterogeneous models is subject to the generation of undesirable errors. These errors are a function of wave nonlinearity and dispersion, and are difficult to quantify directly for model operation. To define validity for practical application, a general benchmark test is proposed with various initial, geometric, and numerical conditions. For this simulation experiment, COMCOT's nonlinear shallow water equation model is coupled with the fully nonlinear version of the Boussinesq model. This approach is taken in order to examine the typical applicability space, since this combination can be regarded as both the most physically well-matched coupling (compared to using the linear COMCOT), and likely also the most common matching setup. The ad hoc modifications presented in Section 5.3 are not used here, to provide a more conservative result. Finally, output from these "validation" simulations are evaluated, with a strong focus on stability and accuracy.

6.1. Gaussian hump simulation

The Gaussian hump initial condition is very useful for this test as the resulting water surface disturbance radiates in all directions, forcing cross-derivatives in the model to be non-zero; there is no dominant propagation direction. The Gaussian hump used here has the initial free surface condition defined as:

$$\zeta(x,y,t) = H_0 \exp\left[-\frac{1}{\alpha^2}\left\{(x-x_0)^2 + (y-y_0)^2\right\}\right], \quad (21)$$

where H_0 is the initial height of the hump at its center (x_0, y_0) and α is the characteristic horizontal lengthscale of the Gaussian hump. All initial velocities are set to zero. The analytical solution for this case can be derived with the assumption of a small amplitude wave, or equivalently a linearization of the governing equations. A solution using Fourier decomposition can be found in Wei and Kirby (1995).

6.2. Physical and numerical setup

The test cases include various physical conditions with different initial H_0/h and α/h, in order to consider the effect of nonlinearity and frequency dispersion on the results. Fig. 7 shows the physical layout of the basin and computational grids. The length of the basin has been fixed at 100 m over all the simulations while the various other parameters are changed. Nonlinearity is expressed in the typical format as $\epsilon = H_0/h$ and dispersion as $\mu = h/L^*$. Here L^*, is a characteristic length scale of the initial condition, given as the length between wave points at 5% H_0, and graphically defined in Fig. 8. The tested range of this parameter is 0.0002–0.0193, a range common for tsunamis where significant dispersion is not expected to be important. μ is not studied in this parametric exercise; these results are only valid for incident long waves where COMCOT can be expected to yield accurate predictions. Nonlinearity ranges from $\epsilon = 0.001$–$\epsilon = 1.0$.

Along with different combinations of physical conditions, numerical parameters are varied as well. These numerical parameters, represented by the grid size ratio between COMCOT and Boussinesq model ($r = \Delta x_C/\Delta x_B$) and the CFL condition $\left(Cr = \sqrt{gh}\Delta t/\Delta x\right)$ are set to cover a wide range of possible configurations. Additionally, the ratio of the Boussinesq grid size to the water depth ($e = \Delta x_B/h$) is tracked to examine some observed instability possibly due to a relatively small Boussinesq grid size.

Consequently, throughout the simulations, four dimensionless parameters (r, ϵ, Cr, and e) are controlled so as to characterize factors affecting the numerical results. Those parameters and their ranges are listed in Table 1, producing 320 unique parameter combinations. For any four parameter set, a simulation is completely described in terms of its physical and numerical configuration.

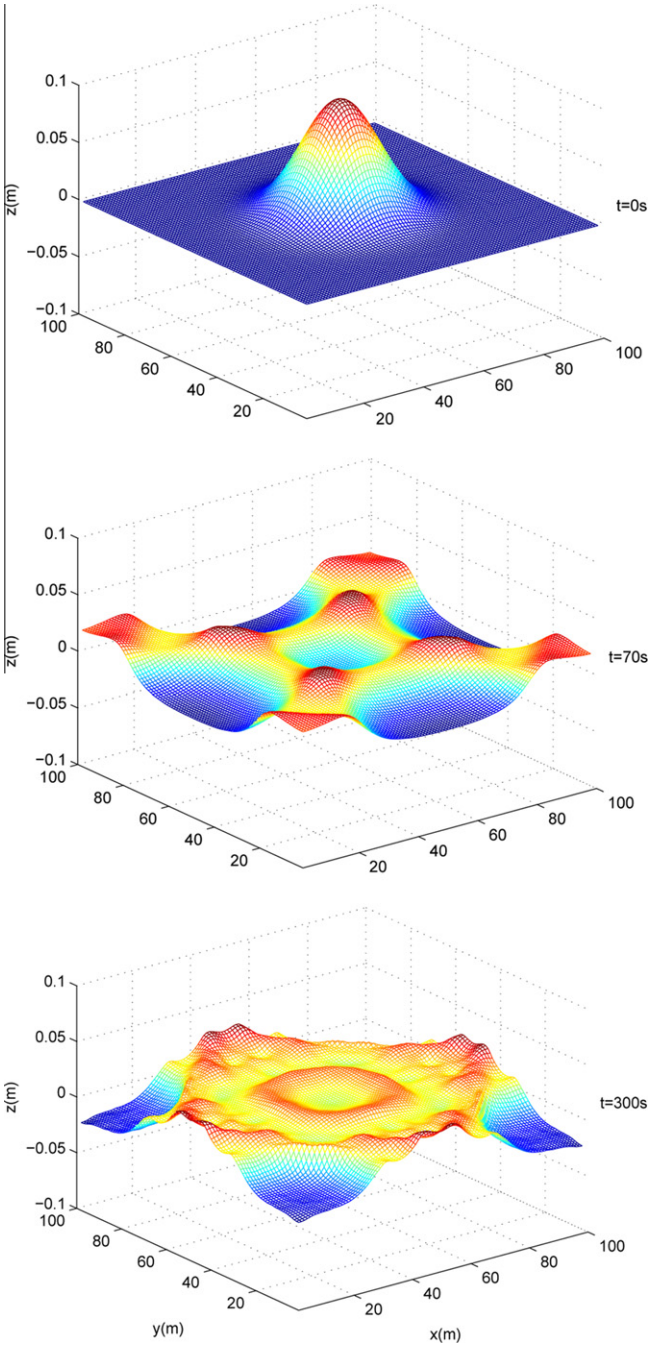

Fig. 10. Snapshots of water surface at 3 different times ($r = 1, \epsilon = 1, Cr = 0.01$ and $e = 10$).

The order by which all the parameters can be calculated is as follows:

1. Calculate Δx_B using r ($\Delta x_C = 1.0$ m, $nx_C = 100$ throughout all the simulations).
2. Next, the number of grid points in the Boussinesq domain can be determined as $nx_B = r \times (50-1) + 1 + 4 + 4$. Note that for imaginary, overlapping grids, 4 grids are added on each edge.
3. Calculate h using e.
4. H_0 can be obtained by $\epsilon (= H_0/h)$.
5. The initial Gaussian surface is generated using $\alpha = 15$ m.
6. Finally, Δt is determined using $Cr\left(=\sqrt{gh}\Delta t/\Delta x_B\right)$.

where Δx, nx denote grid size and grid number, respectively, Δt the time increment, h the water depth, and H_0 the height of hump, respectively. The non-dimensional simulation time, $t'\left(=t\sqrt{gh}/L^*\right) = 30$ has been used for all cases; all individual cases have approximately the same number of water surface fluctuations (characteristic periods) during each simulation.

Among the 320 runs, the most computationally expensive case will be the one with $r = 10$, $Cr = 0.01$, and $\epsilon = 1.0$ which corresponds to $\Delta x_B = 0.1$ m, $\Delta t = 0.01$ s and $nx_B = 499$. On the other hand, the set having $r = 1$, $Cr = 0.5$ and $e = 10$ which gives $\Delta x_B = 1.0$ m, $\Delta t = 0.505$ s and $nx_B = 58$ will be the most rapid. Runs required a few minutes to a few hours to complete on a desktop computer; the longest runs where those which developed numerical instabilities, causing excessive iteration of the Boussinesq corrector step.

6.3. Simulation results

Comparison with an analytical solution is, of course, the ideal method to evaluate the accuracy of a numerical model. However, the aforementioned analytical solution is be obtained using linearization; most of the (ϵ) values tested would violate the required assumption for linearization. Hence, the analytical solution will only be used to show that the coupled numerical model is producing accurate results for the smallest (ϵ) cases. Fig. 9 shows the time series of water surface elevation at the center of the Boussinesq domain when $r = 1$, $\epsilon = 0.001$, $Cr = 0.01$ and $e = 10$. The comparison between numerical and analytical data is excellent for this small amplitude case and the coupled model works quite well. Snapshots of water surface elevation when $r = 1$, $\epsilon = 1$, $Cr = 0.01$ and $e = 10$ are also given in Fig. 10. These snapshots are showing both the Boussinesq and COMCOT surfaces, and there are no evident numerical errors along the interface, or anywhere else in the domain.

Now, interest turns to evaluating output from all 320 simulations in some characteristic way. Here, the time series of surface elevation at the center of the domain will be used as the compar-

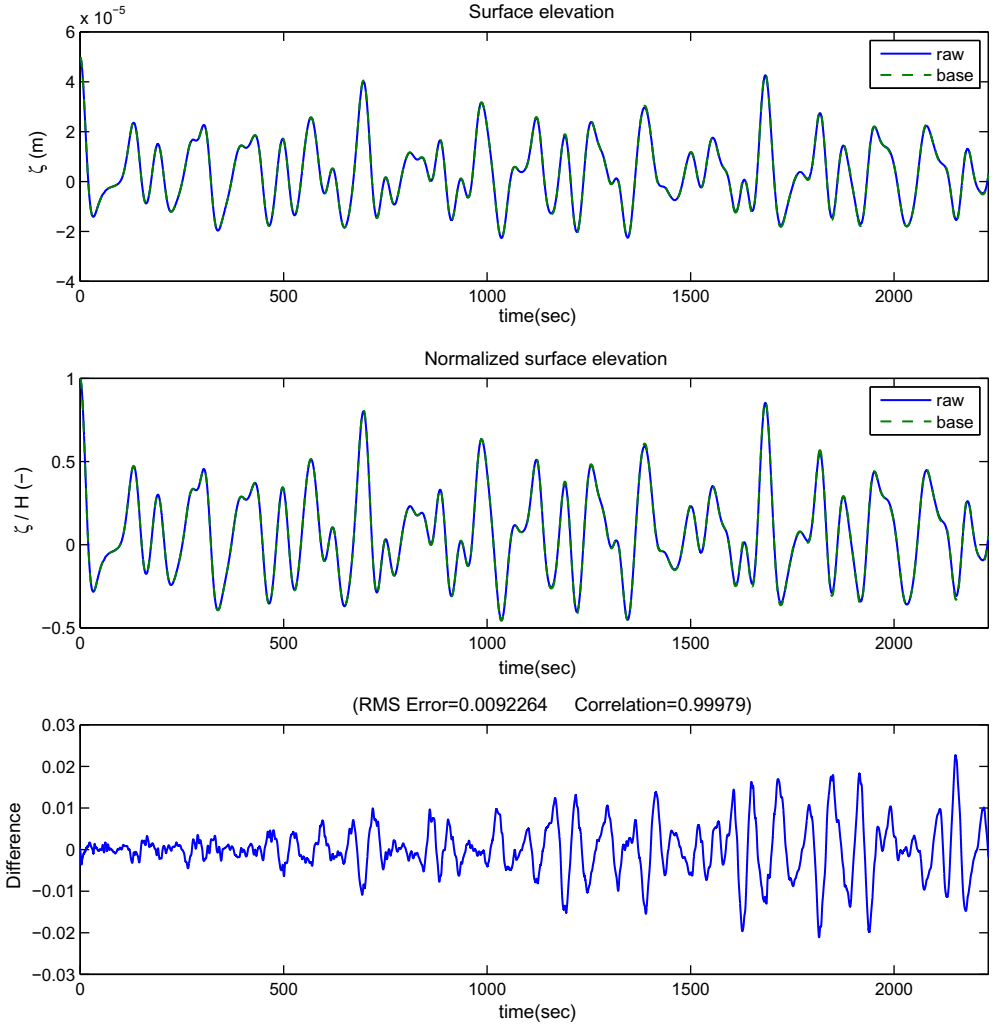

Fig. 11. Calculation of standard deviation when $r = 2$, $\epsilon = 0.001$, $Cr = 0.01$ and $e = 10$.

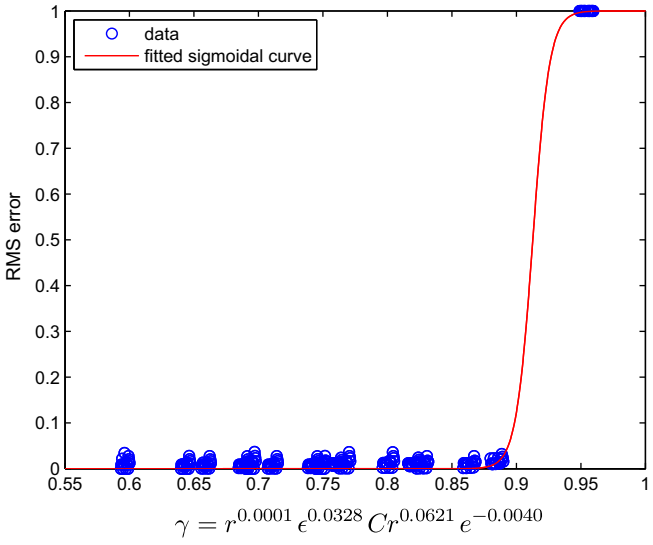

Fig. 12. Error distribution according to stability index, γ, with fitted curve.

ison basis. Considering that use of the linearized analytical solution is not helpful for assessment of highly nonlinear cases, some other available data for accuracy evaluation must be found. Here, a "base" case for each ϵ and μ combination is proposed. Each base case uses $r = 1$ and $Cr = 0.01$, which is expected to produce most accurate and stable result for any physical parameter combination. Therefore, each simulation is able to be evaluated relative to its base case, assumed to be the "correct" solution. Note, however, that with this approach, it is not possible to state with absolute confidence that the "base" case represents an accurate solution, only a stable, converged one. It is likely that stability and accuracy occur in tandem, but this is not guaranteed. Simulations that closely resemble the "base" case can be considered stable simulations, while simulations that do not resemble the "base" case are most likely unstable and inaccurate. Each numerical result is rated with respect to the root mean square (RMS) difference from its base case averaged through the last two dimensionless time units, from $t' = 28$ to *30*. An example depicting this procedure is shown in Fig. 11. Note that if a particular simulation crashes due to instability, this RMS difference is set to 1.0.

Despite the straightforward assessment of the simulation data, it is not a simple matter to demonstrate the relation between the error and the 4 parameters. As indicated in Table 1 and mentioned earlier, the 4 parameters are interrelated, yet affect the results in different ways. For an explicit measure of accuracy and stability using the 4 correlated parameters, a dimensionless parameter, the stability index γ, is introduced. The stability index is a product of r, ϵ ,Cr, and e and is expressed as:

$$\gamma = r^a \epsilon^b Cr^c e^d, \tag{22}$$

where the exponents a, b, c and d are to-be-determined by nonlinear regression analysis on the processed data set. Through the stability index γ, the accuracy and stability properties of a coupled model simulation can be characterized, approximately, before said simulation is run. The higher the γ value, the more poorly behaved the simulation should be. The exponents a, b, c and d are found through a best fit with the RMS error of each simulation; the calibrated stability index should yield the RMS error expected late in a simulation.

Through the nonlinear regression analysis, a, b, c and d are found as 0.0001, 0.0328, 0.0621 and −0.0040, respectively. This implies that the Courant number (Cr) is the most dominant factor in a simulation, whereas the stability of the coupled model is insensitive to both the grid ratio factor (r) and the depth-scaled grid length in the Boussinesq model (e). Fig. 12 shows the error distribution according to γ. It is not surprising that the distribution of RMS error in Fig. 12 resembles a typical cumulative probability curve. There is a transition between stable simulations (RMS error

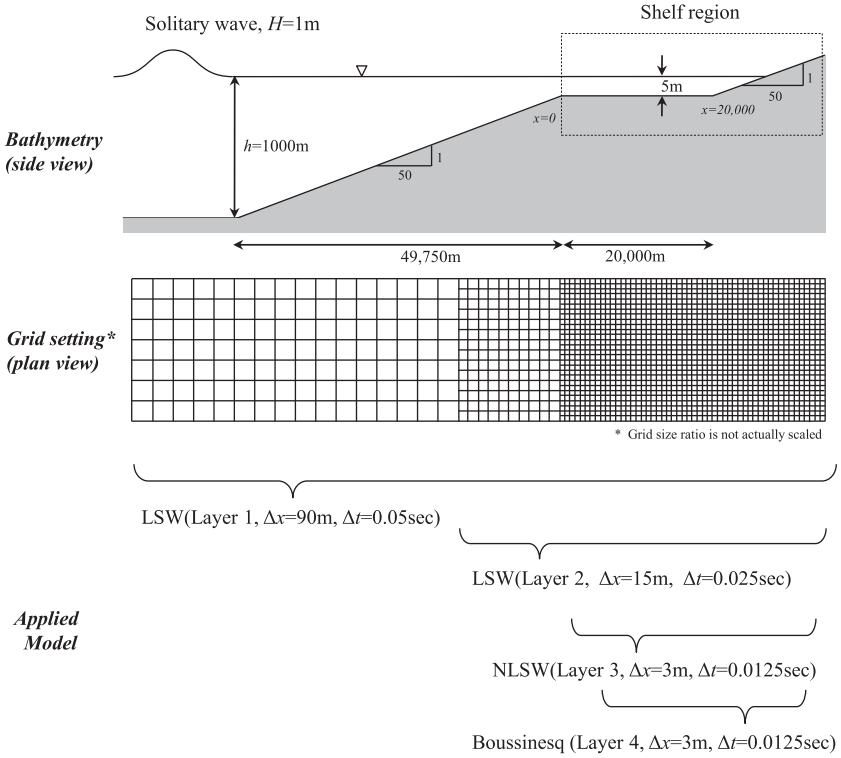

Fig. 13. Definition sketch of a long wave propagating onto a shallow shelf (LSW, linear shallow water equation; NLSW, nonlinear shallow water equation).

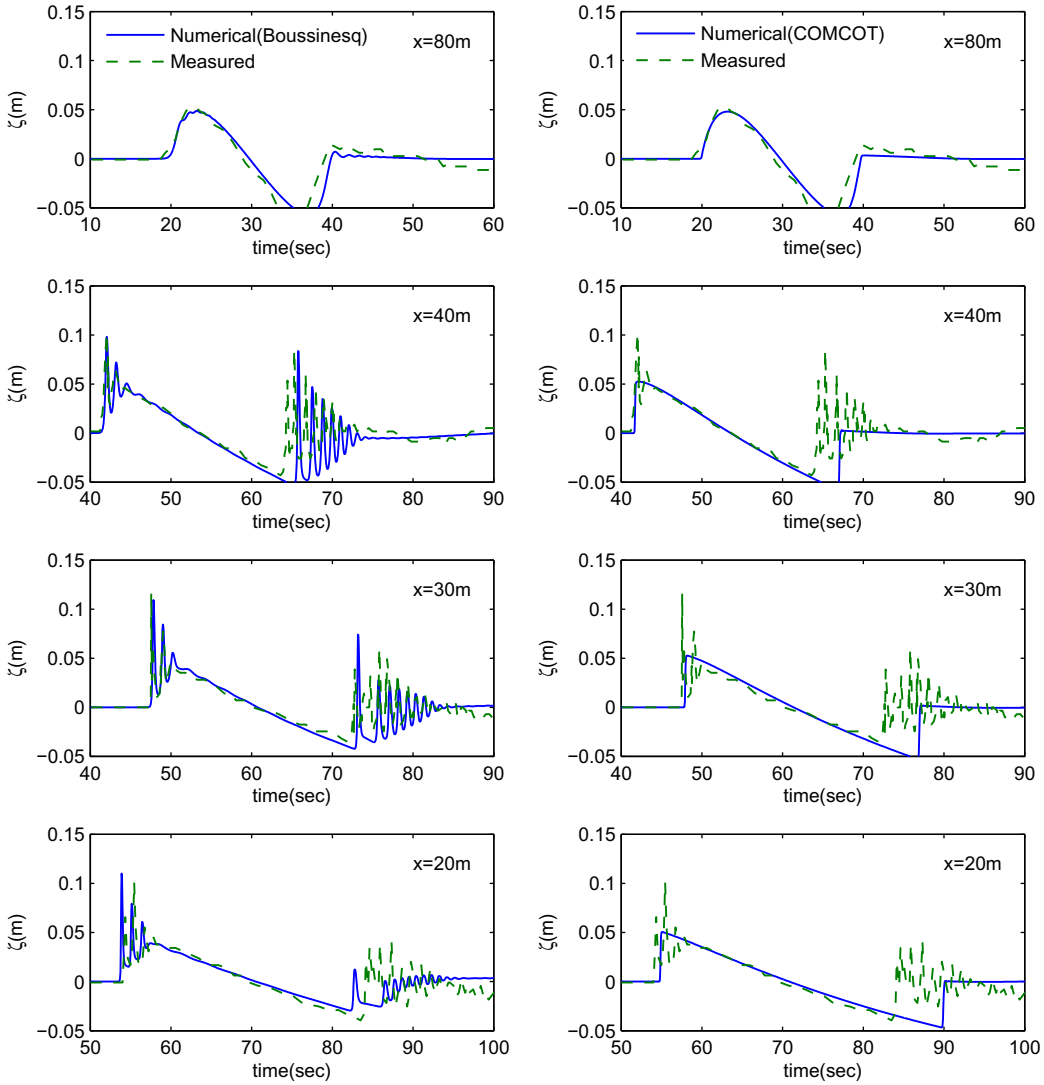

Fig. 14. Time histories of water surface elevations at 4 different locations. In the left half of the figure are shown the coupled model results (solid line: Boussinesq model (Layer 4, dashed line: measured data), while the right half of the figure shows the COMCOT only results at the same times (solid line: nonlinear shallow water equation model (Layer 3), dashed line: measured data).

0) and unstable, inaccurate simulations (RMS error 1), and this error "accumulates" with increasing γ. From this result, it can roughly but conservatively be stated that the stability index γ is recommended to be less than 0.9 to provide a high likelyhood of a stable simulation.

7. Tsunami wave fission simulation

As mentioned in the Introduction, the Boussinesq model has the ability to yield a reasonably complete representation of coastal hydrodynamics. In this section, which is focused on the demonstration of these properties through an efficient use of the coupled model, model verification will be performed using laboratory data. Matsuyama et al. (2007) conducted an experiment in a 205 m long channel using a large and undistorted scale to investigate tsunami shoaling on the continental shelf. The incident waveform uses a sinusoidal-shape wave with single cycle defined as:

$$\zeta = A\sin\left(\frac{2\pi}{T}t\right), \quad 0 \leqslant t \leqslant T$$
$$= 0, \quad t > T \tag{23}$$

where A is wave amplitude, T is period, and t is time. A single experimental case with $A = 0.03$ m and $T = 20$ s, which exhibits significant tsunami shoaling on the continental shelf, is utilized for this study. The experimental set-up is depicted in Fig. 13, where the bathymetry includes a depth-varying shelf connected by two mild-slopes. Long waves from the deep water depth become steeper and possibly short-crested when propagating onto a shallow shelf; nonlinearity and dispersion effects may need to be taken into account for an accurate representation of the long wave transformation.

For the offshore propagation region (Layers 1 and 2), the linear shallow water version of COMCOT is applied using a relatively coarse grid size of 1.5 and 0.3 m, respectively. Along the nearshore area, the nonlinear shallow water equations (Layer 3) are coupled with the Boussinesq model (Layer 4), both using the same relatively fine grid of 0.075 m. Note that a second simulation, without using the Boussinesq model (i.e., Layer 4 removed), was also performed. This will allow for a direct comparison between nearshore predictions of COMCOT and the Boussinesq model, with both using precisely the same incident wave condition and numerical grid sizes. Fig. 14 presents time series comparisons of water surface elevation between the model results and measurements at different

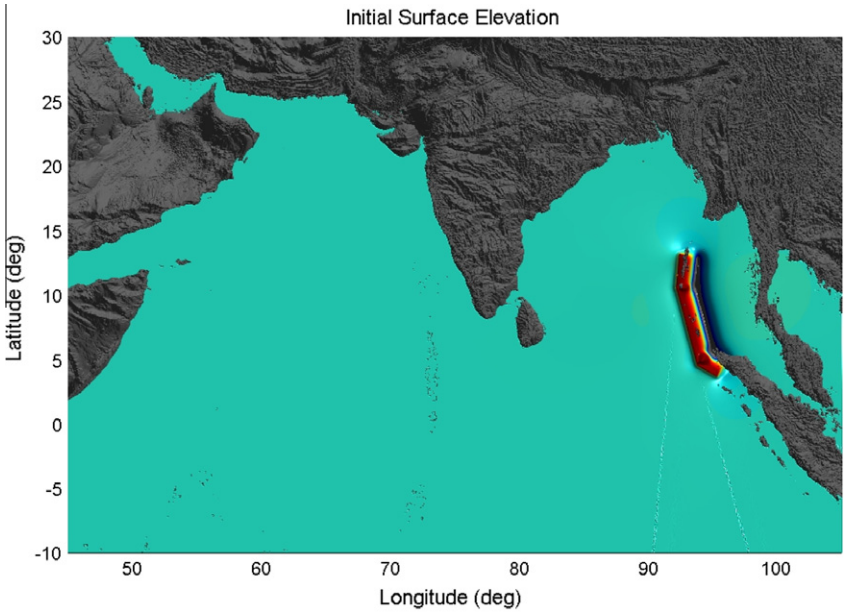

Fig. 15. Initial surface elevation of 2004 Sumatra tsunami.

Table 2
Grid setup for 2004 Sumatra tsunami simulation.

Layer No.	x Range (longitude, °E)	y Range (latitude, °N)	$nx \times ny$	dx	dt(s)	Model
Layer 1	45°00′00″ ~ 105°00′00″	−10°00′00″ ~ 30°00′00″	1801 × 1201	2′	1	LSW (S) [a]
Layer 2	45°17′12″ ~ 61°38′48″	12°17′ 12″ ~ 28°18′48″	2455 × 2405	24″	0.5	LSW (S)
Layer 3	52°56′38″ ~ 56°28′58″	16°08′ 38″ ~ 18°04′58″	2655 × 1455	4.8″	0.25	LSW (S)
Layer 4	53°58′00″ ~ 54°04′00″	16°54′ 00″ ~ 17°00′00″	600 × 600	18.5 m	0.125	NLSW [b]
Layer 5	53°59′46″ ~ 54°01′18″	16°55′ 46″ ~ 16°57′19″	309 × 309	9.3 m	0.125	BOUSS[c]

[a] Linear shallow water model in spherical coordinates.
[b] Non-linear shallow water model in cartesian coordinates.
[c] Boussinesq model in cartesian coordinates.

locations. The coupled model comparisons are given in the left half of the figure, while the COMCOT-only results are shown in the right half. Clearly different behavior of the wave front in the shallow shelf region is predicted by the coupled and COMCOT-only models. The front of the long wave becomes short-crested and generates (or strictly speaking, disintegrates into) several solitons of different size (e.g., Madsen and Mei (1969)); this process is referred to as tsunami wave fission in the literature. This transformation is the classic undular bore formulation which is dispersive in nature, and thus not predictable by the shallow water wave equations solved by COMCOT. The coupled model predicts a maximum sea surface elevation at the front of the tsunami which is 2.0 times larger than COMCOT alone, yielding a good agreement with measured data in both amplitude and speed. This type of difference is highly local in nature, and provides a reasonable picture of the magnitude and scale of dispersion-driven physics during nearshore tsunami evolution.

8. 2004 Sumatra tsunami simulation

As a practical test, the coupled model is applied to the historical tsunami event of December 2004 in the Indian ocean, through which the comprehensive lifespan of a tsunami, from its generation, propagation, shoaling, and run-up, might be investigated in true scale. Our specific geographic focus is Port Salalah, along the southeastern Omani coastline. As noted in the model description, the Boussinesq model enhanced with the viscosity and vorticity terms (i.e., Kim et al., 2009) is capable of simulating turbulence effects such as large eddies and wakes generated in the nearshore or harbors. Hence, another point of interest, aside from the dispersion differences noted in the previous comparison, is predicting such complex turbulent physics, and this is one of the major advantages arising from integrating the two models.

8.1. Simulation setup

The bathymetric data and grid system has been organized to simulate 2004 Sumatra tsunami using the multigrid system in COMCOT. Fig. 15 shows the initial sea surface elevation induced

Table 3
Fault parameters for 2004 Sumatra earthquake.

Parameter	Fault 1	Fault 2	Fault 3
Latitude of epicenter (°N)	7.6	4.15	11.85
Longitude of epicenter (°E)	93	94.55	92.3
Focal depth (km)	5	5	5
Length of fault plane (km)	670	200	300
Width of fault plane (km)	150	150	150
Dislocation (m)	15	15	15
Strike angle (°)	345	300	365
Slip angle (°)	90	90	90
Dip angle (°)	13	13	13

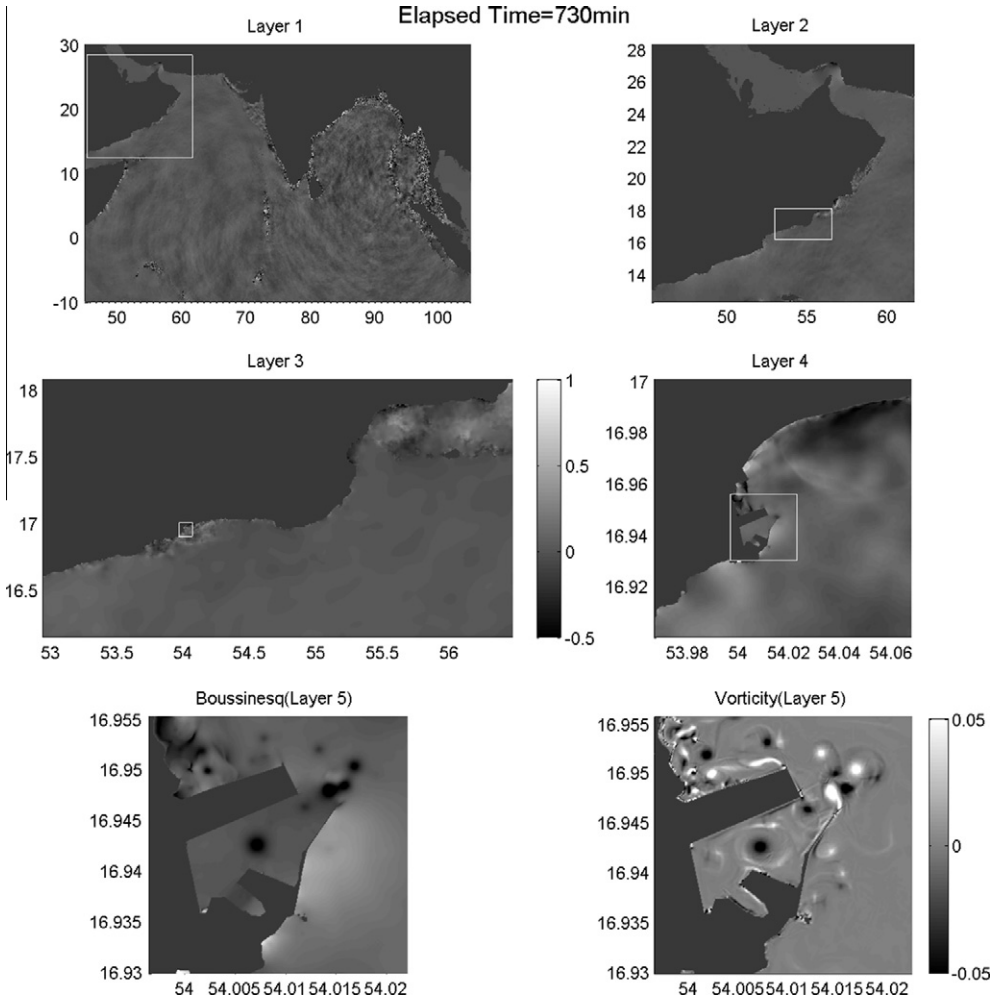

Fig. 16. Surface elevation (m) in all layers at time = 730 min. The lower row shows the output from Layer 5, the Boussinesq model, of the free surface elevation (left) and vorticity (1/s) (right).

by the 2004 Sumatra earthquake within the entire computational domain, covering from (45°E, −10°N) to (105°E, 30°N). Open ocean bathymetry and topography is taken from the GEBCO database, while shallow bathymetry off the coast of Oman is taken from digitized nautical charts. The parent domain, numbered Layer 1, has 4 subdomains given as Layers 2 through 5; higher numbered grids are nested within lower numbered grids. Layer 3, for example, is nested within Layer 2, and has a finer grid size and smaller time step. All the parameters necessary for simulation are listed in Table 2. From Layer 1–4, COMCOT is applied. Near Port Salalah in Oman (Layer 5), the main area of interest, the Boussinesq model with the highest grid resolution is applied in order to capture local and turbulent dynamics, such as vortices, inside the harbor. It is worthwhile to note that the grid resolution is decreased by a factor of 400 from Layers 1 to 5. Additionally, a readily calculated maximum stability index value, γ, is 0.8, assuming that the nonlinearity (ϵ) and water depth are the conservative values of 1 and 23 m, respectively. While this stability index is near the limit of our recommended range, the use of the conservative values implies expected stability for this numerical configuration.

For the generation of an initial surface condition for the tsunami, the three-subfault-source condition of Wang and Liu (2006) has been applied; the parameters of which are listed in Table 3. The runtime of the simulation is set to 830 min of physical time. Additionally, for the purpose of comparison between the results with and without coupling, another simulation using only COMCOT has been implemented with the same configuration except the grid size of Layer 4. In this COMCOT-only simulation, the grid resolution of layer 4 is set to 9.3 m, which is the resolution used by the Boussinesq layer in the coupled model.

8.2. Results and discussion

From the simulation result, the first tsunami waves arrive at Salalah port in Oman (Layer 5) approximately 420 min after the earthquake. This is comparable to the initial arrival time at the Port of 433 minutes post-earthquake, as reported by Okal et al. (2006). Afterward, successive attacks by a long train of tsunami waves caused a significant disturbance inside and immediately near the harbor. These disturbances are given in Okal et al. (2006) who discuss various ship incidents during the tsunami attack. They reported that a freighter docked at the berth had broken its mooring lines and drifted in- and outside the harbor, caught in a complex system of eddies and currents. The coupled model system appears to be able to represent these chaotic dynamics. Fig. 16 shows one result of sea surface in each layer at 730 min after tsunami generation, with an extra plot for the vorticity inside the harbor taken from the Boussinesq layer. Along the breakwater and coastline, the tsunami generates eddies of various sizes, and

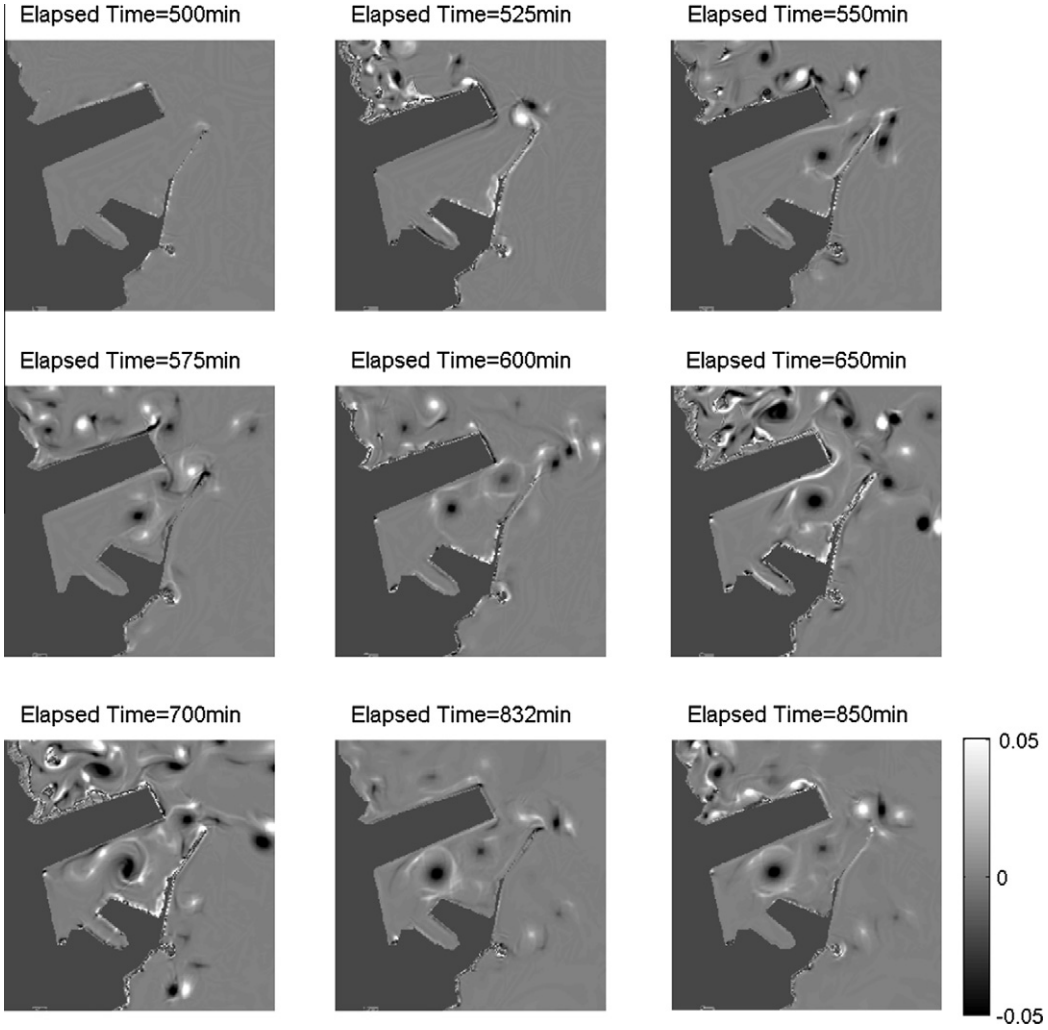

Fig. 17. Vorticity (1/s) evolution inside Oman Salalah harbor at nine different times.

the flow is chaotic. Vorticity evolution as the tsunami propagates into the harbor has been reasonably captured by the Boussinesq model and is depicted in Fig. 17.

A comparison between the vorticity results of COMCOT and the Boussinesq model is shown in Fig. 18. Eddies are very weakly generated in COMCOT relative to the Boussinesq model. While bottom drag, which generates the boundary shear layers that curl up into the large eddies, are modeled differently in the two models, this is likely not the reason for the large difference; for a given velocity the bottom friction from the two formulations will be similar at this geophysical scale. The most likely cause of this large difference is the numerical truncation error of the upwind differencing in COMCOT, given as variable *Er* in Section 4.2. This error can be expressed as:

$$Er = 0.5(1 - Cr)u\Delta x\frac{\partial^2 u}{\partial x^2} = \nu_{\text{num}}\frac{\partial^2 u}{\partial x^2}, \tag{24}$$

and so can clearly be viewed as a diffusion term. For a $Cr \approx 0.5$ and flow speeds ranging from 1 to 5 m/s, the numerical eddy viscosity, ν_{num}, varies from $\approx 2 - 10\,\text{m}^2/\text{s}$. This is a very large diffusion coefficient, and taken with the expectation that the velocity curvature is large inside boundary shear layers and eddies, it is evident that the numerical diffusion in the COMCOT model is driving the large differences in the vorticity patterns. As the two models predict different eddy patterns, the velocity predictions inside the harbor will be equally varied. Specifically, with the large and interacting eddies predicted by the coupled model, the simulated velocities are much larger. This kinematic aspect is of great importance to harbors during tsunamis, as it is the currents that lead to drag forces great enough to snap mooring lines, and transport large freighters as randomly meandering "ghost" ships. If one is interested in simulating these rotational features, numerical errors from low-order upwinding should be avoided.

9. Conclusion

For the purpose of seamlessly modeling tsunami evolution from generation to inundation with fine scale resolution, without the loss of important physics, a two-way coupled model for tsunami simulation has been developed. The two components are the shallow-water solver COMCOT and a dispersive, turbulent, and rotational Boussinesq model. A general framework in which the coupled model is implemented is as follows: Since COMCOT is well designed for generation and propagation of a tsunami in the open ocean, it will be responsible for the computation of oceanic evolution. On the other hand, the final stage of tsunami life, including nearshore dynamics such as inundation, nonlinear

wave interactions, steep bore fronts, and turbulent activity, will be described by a fully nonlinear Boussinesq-type model. The Boussinesq model that can describe nearshore evolution of a tsunami with high physical detail is designed to be located flexibly within COMCOT as a nested layer.

As coupling of two heterogeneous models may result in undesirable errors, a general benchmark test has been completed with various conditions provided for validity of the coupled model application. With regard to stability and accuracy, the simulation output is evaluated and general guidance for the coupled models application space has been presented; the so-called stability index γ should be <0.9. As a further validation of the coupled model in the nearshore region, long wave propagation onto a shallow shelf has been examined and compared with laboratory data. Distinct dispersive effects at the leading wave front have been observed through use of the Boussinesq model, which demonstrates that near coastal areas, dispersive effects may be locally important.

Finally, a recent tsunami event, the 2004 Sumatra tsunami, has been simulated with a far field focus on the Port of Salalah. The coupled model has successfully simulated various sizes of eddies generated by the tsunami through turbulence activity. The results are further supported by observations addressed in Okal et al. (2006). It is found that one needs to be very careful when using numerical solution schemes with leading order diffusion errors to predict such rotational features, as this numerical error can rapidly remove intense shear layers and strong eddies from the current field.

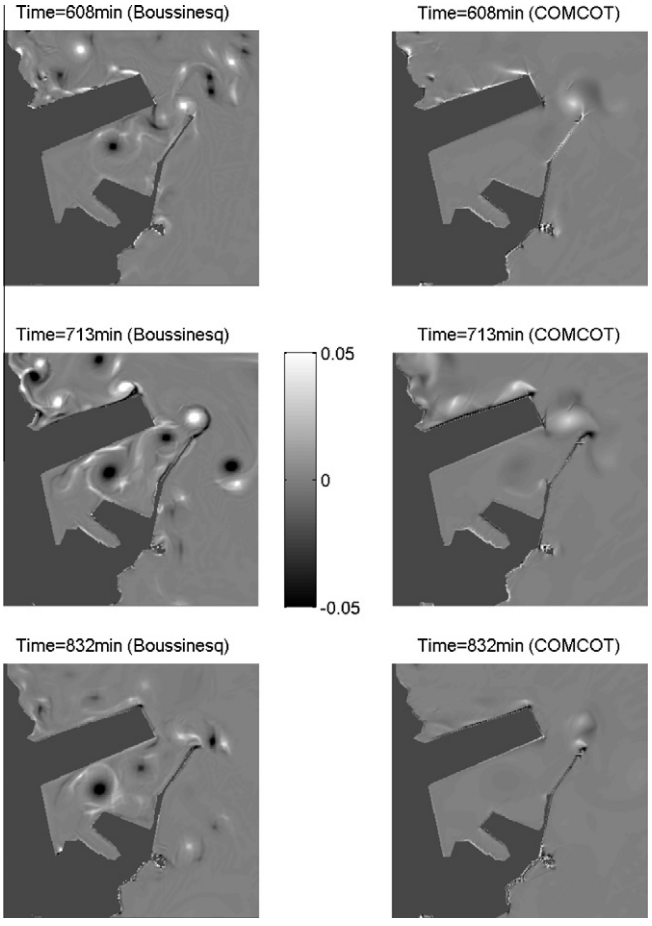

Fig. 18. Comparison of vorticity (1/s) evolution by Boussinesq-coupled model (left) and COMCOT-only (right).

Acknowledgements

The research presented here was partially supported by a grant from Lighthouse R&D Enterprises, Inc. to Texas A&M University.

Appendix A. Numerical scheme of COMCOT

The numerical solution scheme employed by COMCOT is the explicit leap-frog difference method. Nonlinear terms in the model are approximated with upwind finite differences. The final forms for the continuity and momentum equations are described below:

$$\zeta_{i,j}^{n+1/2} = \zeta_{i,j}^{n-1/2} - \frac{\Delta t}{\Delta x}\left(M_{i+1/2,j}^{n} - M_{i-1/2,j}^{n}\right) - \frac{\Delta t}{\Delta y}\left(N_{i,j+1/2}^{n} - N_{i,j-1/2}^{n}\right), \tag{25}$$

$$\begin{aligned} M_{i+1/2,j}^{n+1} = {} & \frac{1}{1+v_x\Delta t}\left[(1-v_x\Delta t)M_{i+1/2,j}^{n} - g\frac{\Delta t}{\Delta x}H_{i+1/2,j}^{n+1/2}\left(\zeta_{i+1,j}^{n+1/2} - \zeta_{i,j}^{n+1/2}\right)\right] \\ & - \frac{\Delta t}{\Delta x(1+v_x\Delta t)}\left[\lambda_{11}\frac{\left(M_{i+3/2,j}^{n}\right)^2}{H_{i+3/2,j}^{n}} + \lambda_{12}\frac{\left(M_{i+1/2,j}^{n}\right)^2}{H_{i+1/2,j}^{n}} + \lambda_{13}\frac{\left(M_{i-1/2,j}^{n}\right)^2}{H_{i-1/2,j}^{n}}\right] \\ & - \frac{\Delta t}{\Delta y(1+v_x\Delta t)}\left[\lambda_{21}\frac{(MN)_{i+1/2,j+1}^{n}}{H_{i+1/2,j+1}^{n}} + \lambda_{22}\frac{(MN)_{i+1/2,j}^{n}}{H_{i+1/2,j}^{n}} + \lambda_{23}\frac{(MN)_{i+1/2,j-1}^{n}}{H_{i+1/2,j-1}^{n}}\right], \end{aligned} \tag{26}$$

$$\begin{aligned} N_{i,j+1/2}^{n+1} = {} & \frac{1}{1+v_y\Delta t}\left[(1-v_y\Delta t)N_{i,j+1/2}^{n} - g\frac{\Delta t}{\Delta y}H_{i,j+1/2}^{n+1/2}\left(\zeta_{i,j+1}^{n+1/2} - \zeta_{i,j}^{n+1/2}\right)\right] \\ & - \frac{\Delta t}{\Delta x(1+v_y\Delta t)}\left[\lambda_{31}\frac{(MN)_{i+1,j+1/2}^{n}}{H_{i+1,j+1/2}^{n}} + \lambda_{32}\frac{(MN)_{i,j+1/2}^{n}}{H_{i,j+1/2}^{n}} + \lambda_{33}\frac{(MN)_{i-1,j+1/2}^{n}}{H_{i-1,j+1/2}^{n}}\right] \\ & - \frac{\Delta t}{\Delta y(1+v_y\Delta t)}\left[\lambda_{41}\frac{\left(N_{i,j+3/2}^{n}\right)^2}{H_{i,j+3/2}^{n}} + \lambda_{42}\frac{\left(N_{i,j+1/2}^{n}\right)^2}{H_{i,j+1/2}^{n}} + \lambda_{43}\frac{\left(N_{i,j-1/2}^{n}\right)^2}{H_{i,j-1/2}^{n}}\right], \end{aligned} \tag{27}$$

where the coefficients of the upwind scheme are obtained by

$$\begin{cases} \lambda_{11}=0, & \lambda_{12}=1, & \lambda_{13}=-1, & \text{if } M_{i+1/2,j}^{n} \geqslant 0, \\ \lambda_{11}=1, & \lambda_{12}=-1, & \lambda_{13}=0, & \text{if } M_{i+1/2,j}^{n} < 0, \end{cases}$$

$$\begin{cases} \lambda_{21}=0, & \lambda_{22}=1, & \lambda_{23}=-1, & \text{if } N_{i+1/2,j}^{n} \geqslant 0, \\ \lambda_{21}=1, & \lambda_{22}=-1, & \lambda_{23}=0, & \text{if } N_{i+1/2,j}^{n} < 0, \end{cases}$$

$$\begin{cases} \lambda_{31}=0, & \lambda_{32}=1, & \lambda_{33}=-1, & \text{if } M_{i,j+1/2}^{n} \geqslant 0, \\ \lambda_{31}=1, & \lambda_{32}=-1, & \lambda_{33}=0, & \text{if } M_{i,j+1/2}^{n} < 0, \end{cases}$$

$$\begin{cases} \lambda_{41}=0, & \lambda_{42}=1, & \lambda_{43}=-1, & \text{if } N_{ij+1/2}^{n} \geqslant 0, \\ \lambda_{41}=1, & \lambda_{42}=-1, & \lambda_{43}=0, & \text{if } N_{i,j+1/2}^{n} < 0. \end{cases}$$

Bottom friction terms are given as:

$$v_x = \frac{1}{2}\frac{gm^2}{\left(H_{i+1/2,j}^{n}\right)^{7/3}}\left[\left(M_{i+1/2,j}^{n}\right)^2 + \left(N_{i+1/2,j}^{n}\right)^2\right]^{1/2}, \tag{28}$$

$$v_y = \frac{1}{2}\frac{gm^2}{\left(H_{ij+1/2}^{n}\right)^{7/3}}\left[\left(M_{ij+1/2}^{n}\right)^2 + \left(N_{ij+1/2}^{n}\right)^2\right]^{1/2}. \tag{29}$$

Appendix B. Parameters in Boussinesq model

B.1. 2nd order terms in Boussinesq equation

$$D_c = -\nabla\cdot\left[(\zeta+h)\left\{\left(\frac{\left(\zeta^2-\zeta h+h^2\right)}{6}-\frac{z_\alpha^2}{2}\right)\nabla S+\left(\frac{(\zeta-h)}{2}-z_\alpha\right)\nabla T\right\}\right] + \nabla\cdot\left[\boldsymbol{\psi}(\zeta+h)\left\{\frac{z_\alpha^2}{2}-z_\alpha\zeta+\frac{\left(2\zeta^2-2\zeta h-h^2\right)}{6}\right\}\right], \tag{30}$$

$$\left(D_m^x, D_m^y\right) = \boldsymbol{D}+\boldsymbol{D}^v+\bar{\boldsymbol{\xi}}+\overline{\boldsymbol{\xi}^v}-\nabla\cdot\left(\nu_t^h\nabla\boldsymbol{U}_\alpha\right)+\nu_t^v\nabla S+\frac{\boldsymbol{\tau}_b}{\rho H}, \tag{31}$$

$$\begin{aligned}\boldsymbol{D} = {}& \frac{1}{2}\nabla\left(z_\alpha^2\boldsymbol{U}_\alpha\cdot\nabla S\right)+\nabla\left(z_\alpha\boldsymbol{U}_\alpha\cdot\nabla T\right)+\left(T\nabla T\right)-\frac{1}{2}\nabla\left(\zeta^2\frac{\partial S}{\partial t}\right)\\ & -\nabla\left(\zeta\frac{\partial T}{\partial t}\right)+\left(\frac{1}{2}z_\alpha^2\frac{\partial\nabla S}{\partial t}+z_\alpha\frac{\partial\nabla T}{\partial t}\right)-\frac{1}{2}\nabla\left(\zeta^2\boldsymbol{U}_\alpha\cdot\nabla S\right)\\ & -\nabla\left(\zeta\boldsymbol{U}_\alpha\cdot\nabla T\right)+\nabla\left(\frac{1}{2}\zeta^2S^2\right)+\nabla\left(\zeta TS\right),\end{aligned} \tag{32}$$

$$\begin{aligned}\boldsymbol{D}^v = {}& \frac{(\zeta-h)}{2}\frac{\partial\boldsymbol{\psi}\zeta}{\partial t}-\frac{\left(\zeta^2-\zeta h+h^2\right)}{6}\frac{\partial\boldsymbol{\psi}}{\partial t}\\ & +\frac{\partial}{\partial t}\left\{\boldsymbol{\psi}\left(\frac{z_\alpha^2}{2}-\zeta z_\alpha\right)\right\}+\frac{(\zeta-h)}{2}\nabla\left\{\boldsymbol{U}_\alpha\cdot(\boldsymbol{\psi}\zeta)\right\}\\ & -\frac{\left(\zeta^2-\zeta h+h^2\right)}{6}\nabla\left(\boldsymbol{U}_\alpha\cdot\boldsymbol{\psi}\right)+\nabla\left[\boldsymbol{U}_\alpha\cdot\left\{\boldsymbol{\psi}\left(\frac{z_\alpha^2}{2}-\zeta z_\alpha\right)\right\}\right]\\ & -\boldsymbol{\psi}\left\{\frac{\left(\zeta^2+\zeta h-2h^2\right)S}{6}+\frac{(\zeta+h)T}{2}\right\},\end{aligned} \tag{33}$$

where $\nabla = (\partial/\partial x, \partial/\partial y)$, $S = \nabla\cdot\boldsymbol{U}_\alpha$, $T = \nabla\cdot(h\boldsymbol{U}_\alpha)$ and $\boldsymbol{\psi} = \boldsymbol{\tau}_b/\{\rho\nu_t^v(\zeta+h)\}$. Also $\bar{\boldsymbol{\xi}} = (\overline{\xi^x}, \overline{\xi^y})$ and $\overline{\boldsymbol{\xi}^v} = (\overline{\xi^{vx}}, \overline{\xi^{vy}})$ are given by

$$\begin{aligned}\overline{\xi^x} = {}& -V_\alpha\left\{\frac{\partial z_\alpha}{\partial x}\left(z_\alpha\frac{\partial S}{\partial y}+\frac{\partial T}{\partial y}\right)-\frac{\partial z_\alpha}{\partial y}\left(z_\alpha\frac{\partial S}{\partial x}+\frac{\partial T}{\partial x}\right)\right\}\\ & -\left(\frac{\partial V_\alpha}{\partial x}-\frac{\partial U_\alpha}{\partial y}\right)\left[\left\{\frac{z_\alpha^2}{2}-\frac{\left(\zeta^2-\zeta h+h^2\right)}{6}\right\}\frac{\partial S}{\partial y}+\left\{z_\alpha-\frac{(\zeta-h)}{2}\right\}\frac{\partial T}{\partial y}\right],\end{aligned} \tag{34}$$

$$\begin{aligned}\overline{\xi^y} = {}& U_\alpha\left\{\frac{\partial z_\alpha}{\partial x}\left(z_\alpha\frac{\partial S}{\partial y}+\frac{\partial T}{\partial y}\right)-\frac{\partial z_\alpha}{\partial y}\left(z_\alpha\frac{\partial S}{\partial x}+\frac{\partial T}{\partial x}\right)\right\}\\ & +\left(\frac{\partial V_\alpha}{\partial x}-\frac{\partial U_\alpha}{\partial y}\right)\left[\left\{\frac{z_\alpha^2}{2}-\frac{\left(\zeta^2-\zeta h+h^2\right)}{6}\right\}\frac{\partial S}{\partial x}+\left\{z_\alpha-\frac{(\zeta-h)}{2}\right\}\frac{\partial T}{\partial x}\right],\end{aligned} \tag{35}$$

$$\begin{aligned}\overline{\xi^{vx}} = {}& -V_\alpha\left[\frac{\partial}{\partial x}\left\{\psi^y\left(\frac{1}{2}z_\alpha^2-z_\alpha\zeta\right)\right\}-\frac{\left(\zeta^2-\zeta h+h^2\right)}{6}\frac{\partial\psi^y}{\partial x}+\frac{(\zeta-h)}{2}\frac{\partial\psi^y\zeta}{\partial x}\right.\\ & \left.-\frac{\partial}{\partial y}\left\{\psi^x\left(\frac{1}{2}z_\alpha^2-z_\alpha\zeta\right)\right\}+\frac{\left(\zeta^2-\zeta h+h^2\right)}{6}\frac{\partial\psi^x}{\partial y}-\frac{(\zeta-h)}{2}\frac{\partial\psi^x\zeta}{\partial y}\right]\\ & -\left(\frac{\partial V_\alpha}{\partial x}-\frac{\partial U_\alpha}{\partial y}\right)\psi^y\left\{\frac{z_\alpha^2}{2}-z_\alpha\zeta+\frac{\left(2\zeta^2-2\zeta h-h^2\right)}{6}\right\},\end{aligned} \tag{36}$$

$$\begin{aligned}\overline{\xi^{vy}} = {}& U_\alpha\left[\frac{\partial}{\partial x}\left\{\psi^y\left(\frac{1}{2}z_\alpha^2-z_\alpha\zeta\right)\right\}-\frac{\left(\zeta^2-\zeta h+h^2\right)}{6}\frac{\partial\psi^y}{\partial x}+\frac{(\zeta-h)}{2}\frac{\partial\psi^y\zeta}{\partial x}\right.\\ & \left.-\frac{\partial}{\partial y}\left\{\psi^x\left(\frac{1}{2}z_\alpha^2-z_\alpha\zeta\right)\right\}+\frac{\left(\zeta^2-\zeta h+h^2\right)}{6}\frac{\partial\psi^x}{\partial y}-\frac{(\zeta-h)}{2}\frac{\partial\psi^x\zeta}{\partial y}\right]\\ & +\left(\frac{\partial V_\alpha}{\partial x}-\frac{\partial U_\alpha}{\partial y}\right)\psi^x\left\{\frac{z_\alpha^2}{2}-z_\alpha\zeta+\frac{\left(2\zeta^2-2\zeta h-h^2\right)}{6}\right\},\end{aligned} \tag{37}$$

and $(\psi^x, \psi^y) = \boldsymbol{\psi}$.

B.2. Variables in numerical scheme

$$E = E_{LO}+E_D+E_V, \tag{38}$$

$$F = F_{LO}+F_D+U_\alpha(E_D+E_V), \tag{39}$$

$$G = G_{LO}+G_D+V_\alpha(E_D+E_V), \tag{40}$$

E_{LO}, F_{LO}, and G_{LO} are rewritten by

$$E_{LO} = -\frac{\partial HU_\alpha}{\partial x}-\frac{\partial HV_\alpha}{\partial y}, \tag{41}$$

$$F_{LO} = -\frac{\partial}{\partial x}\left(HU_\alpha^2+\frac{1}{2}gH^2\right)-\frac{\partial HU_\alpha V_\alpha}{\partial y}+gH\frac{\partial h}{\partial x}, \tag{42}$$

$$G_{LO} = -\frac{\partial HU_\alpha V_\alpha}{\partial x}-\frac{\partial}{\partial y}\left(HV_\alpha^2+\frac{1}{2}gH^2\right)+gH\frac{\partial h}{\partial y}, \tag{43}$$

and E_D, E_V, F_D, G_D, F_1 and G_1 are defined as:

$$E_D = \left[H\left\{\left(\frac{1}{6}\left(\zeta^2-\zeta h+h^2\right)-\frac{1}{2}z_\alpha^2\right)\nabla S+\left(\frac{1}{2}(\zeta-h)-z_\alpha\right)\nabla T\right\}\right]_x + \left[H\left\{\left(\frac{1}{6}\left(\zeta^2-\zeta h+h^2\right)-\frac{1}{2}z_\alpha^2\right)\nabla S+\left(\frac{1}{2}(\zeta-h)-z_\alpha\right)\nabla T\right\}\right]_y, \tag{44}$$

$$E_V = -\left[H\psi^x\left\{\frac{z_\alpha^2}{2}-z_\alpha\zeta+\frac{\left(2\zeta^2-2\zeta h-h^2\right)}{6}\right\}\right]_x - \left[H\psi^y\left\{\frac{z_\alpha^2}{2}-z_\alpha\zeta+\frac{\left(2\zeta^2-2\zeta h-h^2\right)}{6}\right\}\right]_y, \tag{45}$$

$$\begin{aligned}(F_D, G_D) = H\Bigg[& \frac{1}{2}\nabla\left(\zeta^2\mathbf{U}_\alpha\cdot\nabla S\right)+\nabla\left(\zeta\mathbf{U}_\alpha\cdot\nabla T\right)-\frac{1}{2}\nabla\left(\zeta^2S^2\right)\\ & -\frac{1}{2}\nabla\left(z_\alpha^2\mathbf{U}_\alpha\cdot\nabla S\right)-\nabla\left(z_\alpha\mathbf{U}_\alpha\cdot\nabla T\right)-\left(T\nabla T\right)\\ & -\nabla\left(\zeta TS\right)-\frac{(\zeta-h)}{2}\nabla\left\{\mathbf{U}_\alpha\cdot(\boldsymbol{\psi}\zeta)\right\}\\ & +\frac{\left(\zeta^2-\zeta h+h^2\right)}{6}\nabla\left(\mathbf{U}_\alpha\cdot\boldsymbol{\psi}\right)-\nabla\left[\mathbf{U}_\alpha\cdot\left\{\boldsymbol{\psi}\left(\frac{z_\alpha^2}{2}-\zeta z_\alpha\right)\right\}\right]\\ & +\boldsymbol{\psi}\left\{\frac{\left(\zeta^2+\zeta h-2h^2\right)S}{6}+\frac{HT}{2}\right\}-\bar{\boldsymbol{\xi}}-\overline{\boldsymbol{\xi}^v}\\ & +\nabla\cdot\left(\nu_t^h\nabla\mathbf{U}_\alpha\right)-\nu_t^v\nabla S-\frac{\boldsymbol{\tau}_b}{\rho H}\Bigg],\end{aligned} \tag{46}$$

$$F_1 = \frac{H}{2}\left(\zeta^2-z_\alpha^2\right)V_{\alpha xy}-H(z_\alpha-\zeta)(hV_\alpha)_{xy}+H\zeta_x\left\{\zeta V_{\alpha y}+(hV_\alpha)_y\right\}, \tag{47}$$

$$G_1 = \frac{H}{2}\left(\zeta^2-z_\alpha^2\right)U_{\alpha xy}-H(z_\alpha-\zeta)(hU_\alpha)_{xy}+H\zeta_y\left\{\zeta U_{\alpha x}+(hU_\alpha)_x\right\}, \tag{48}$$

F_v^p, G_v^p, F_v^c and G_v^c are rewritten by

$$F_v^p = \frac{H^n\left(\zeta^2 - \zeta h + h^2 + 3z_\alpha^2\right)^n}{6}\left\{2(\psi^x)^n - 3(\psi^x)^{n-1} + (\psi^x)^{n-2}\right\} - \frac{H^n(\zeta - h - 2z_\alpha)^n}{2}\left\{2(\psi^x\zeta)^n - 3(\psi^x\zeta)^{n-1} + (\psi^x\zeta)^{n-2}\right\} \quad (49)$$

$$G_v^p = \frac{H^n\left(\zeta^2 - \zeta h + h^2 + 3z_\alpha^2\right)^n}{6}\left\{2(\psi^y)^n - 3(\psi^y)^{n-1} + (\psi^y)^{n-2}\right\} - \frac{H^n(\zeta - h - 2z_\alpha)^n}{2}\left\{2(\psi^y\zeta)^n - 3(\psi^y\zeta)^{n-1} + (\psi^y\zeta)^{n-2}\right\} \quad (50)$$

$$F_v^c = \frac{H^{n+1}\left(\zeta^2 - \zeta h + h^2 + 3z_\alpha^2\right)^{n+1}}{6}\left\{(\psi^x)^{n+1} - (\psi^x)^n\right\} - \frac{H^{n+1}(\zeta - h - 2z_\alpha)^{n+1}}{2}\left\{(\psi^x\zeta)^{n+1} - (\psi^x\zeta)^n\right\} \quad (51)$$

$$G_v^c = \frac{H^{n+1}\left(\zeta^2 - \zeta h + h^2 + 3z_\alpha^2\right)^{n+1}}{6}\left\{(\psi^y)^{n+1} - (\psi^y)^n\right\} - \frac{H^{n+1}(\zeta - h - 2z_\alpha)^{n+1}}{2}\left\{(\psi^y\zeta)^{n+1} - (\psi^y\zeta)^n\right\} \quad (52)$$

References

Burwell, D., Tolkova, E., Chawla, A., 2007. Diffusion and dispersion characterization of a numerical tsunami model. Ocean Modell. 19 (1–2), 10–30.

George, D.L., LeVeque, R.J., 2006. Finite volume methods and adaptive refinement for global tsunami propagation and local inundation. Sci. Tsunami Hazards 24, 319–328.

Gobbi, M.F., Kirby, J.T., 1999. Wave evolution over submerged sills: tests of a high-order Boussinesq model. Coast. Eng. 37, 57–96.

Grilli, S.T., Ioualalen, M., Asavanant, J., Shi, F., Kirby, J., Watts, P., 2007. Source constraints and model simulation of the December 26, 2004 Indian Ocean tsunami. J. Waterw. Port Coastal Ocean Eng. 133 (6), 414–428.

Harig, S., Chaeroni, C., Pranowo, W.S., Behrens, J., 2008. Tsunami simulations on several scales: comparison of approaches with unstructured meshes and nested grids. Ocean Dynam. 58, 429–440.

Kim, D.-H., Lynett, P., Socolofsky, S., 2009. A depth-integrated model for weakly dispersive, turbulent, and rotational fluid flows. Ocean Modell. 27 (3-4), 198–214.

Kowalik, Z., Knight, W., Logan, T., Whitmore, P., 2005. Numerical modeling of the global tsunami: Indonesian tsunami of 26 December 2004. Sci. Tsunami Hazards 23 (1), 40–56.

Liu, P.L.-F., Woo, S.B., Cho, Y.S. 1998. Computer programs for tsunami propagation and inundation, Technical report, Cornell University.

Lynett, P., Borrero, J., Liu, P.L.-F., Synolakis, C.E., 2003. Field survey and numerical simulations: a review of the 1998 Papua New Guinea tsunami. Pure Appl. Geophys. 160, 2119–2146.

Lynett, P., 2006. Nearshore wave modeling with high-order Boussinesq-type equations. J. Waterw. Port Coastal Ocean Eng. 132 (5), 348–357.

Madsen, O.S., Mei, C.C., 1969. The transformation of a solitary wave over an uneven bottom. J. Fluid Mech. 39, 781–791.

Matsuyama, M., Ikeno, M., Sakakiyama, T., Takeda, T., 2007. A study of tsunami wave fission in an undistorted experiment. Pure Appl. Geophys. 164, 617–631.

Okada, Y., 1985. Surface deformation to shear and tensile faults in a half-space. Bull. Seismol. Soc. Am. 75, 1135–1154.

Okal, E.A., Fritz, H.M., Raad, P.E., Synolakis, C.E., Al-Shijbi, Y., Al-Saifi, M., 2006. Oman field survey after the December 2004 Indian Ocean tsunami. Earthquake Spectra 22, S203–S218.

Saito, T., Furumura, T., 2009. Three-dimensional simulation of tsunami generation and propagation: application to Intraplate events. J. Geophys. Res. 114, B02307.

Shapiro, R., 1970. Smoothing, filtering, and boundary effects. Rev. Geophys. Space Phys. 8 (2), 359–387.

Titov, V.V., Synolakis, C.E., 1998. Numerical modeling of tidal wave runup. J. Waterw. Port Coastal Ocean Eng. 124 (4), 157–171.

Wang, X., Liu, P.L.-F., 2006. An analysis of 2004 Sumatra earthquake fault plane mechanisms and Indian Ocean tsunami. J. Hydraul. Res. 44 (2), 147–154.

Wei, G., Kirby, J.T., 1995. A time-dependent numerical code for extended Boussinesq equations. J. Waterw. Port Coastal Ocean Eng. 121, 251–261.

Yoon, S.B., 2002. Propagation of distant tsunamis over slowly varying topography. J. Geophys. Res. 107 (C10), 3140.